© Copyright 2021

Laura Ann Carlucci

The unusual strength of the FimH catch bond under force

Laura Ann Carlucci

A dissertation

submitted in partial fulfillment of the

requirements for the degree of

Doctor of Philosophy

University of Washington

2021

Reading Committee:

Wendy Thomas, Chair

Rachel Klevit

Paul Wiggins

Program Authorized to Offer Degree:

Bioengineering

University of Washington

Abstract

The unusual strength of the FimH catch bond under force

Laura Ann Carlucci

Chair of the Supervisory Committee:
Professor Wendy Thomas
Bioengineering

Many receptor ligand interactions have developed catch bond properties to overcome and even utilize forces that may oppose the attachment. The lifetime of a catch bond increases under force. FimH is an *E. coli* adhesive protein that forms a catch bond with mannose via a force-induced transition from a low-ligand-affinity state to a high-affinity state. The high-affinity state possesses incredibly strong binding properties that have never been fully characterized.

In this work we sought to measure the lifetime of FimH in the high-affinity state using a constant force assay on a multiplexed magnetic tweezers. The magnetic tweezer applies a constant force to the bond between an anchored receptor and a ligand-coated bead. The applied force can vary between beads and is estimated from the velocity of the untethered bead along the focal axis. Movement in this direction requires analysis of diffraction rings whose pattern depends on the z-position of the bead. These are compared to diffraction ring images of beads

taken at known z-locations. However, we often encountered errors in bead positions that could not be attributed to anything other than the tracking. By repeatedly manipulating a magnetic bead between a chamber floor and ceiling we found our bead tracking method resulted in unexpectedly high variability in the estimated bead positions and velocity. We found that excluding the center-most diffraction rings significantly improved the precision of bead tracking.

With this new tracking method, we then measured the lifetime of the high-affinity state of FimH under force. We found the lifetime to be incredibly long, yet the rates of unbinding could not described by the expected single exponential decay model, but rather a double exponential decay model – suggesting multi-state unbinding kinetics. While this behavior could be the result of the magnetic beads forming multiple fimbria attachments, this explanation is highly unlikely as the effect of force on the rate of unbinding is not what we would expect if multiple bonds were forming. Rather it appears the FimH-mannose bond has at least two different states upon force activation. These results are the first functional evidence demonstrating this heterogeneous behavior.

TABLE OF CONTENTS

LIST OF FIGURES

ACKNOWLEDGEMENTS

This journey was not one I could have completed alone. The people I met in Seattle have helped me grow as a researcher, a scientist, a colleague, and a person.

To start, I'd like to thank my advisor, Wendy Thomas who always believed in me even when I didn't believe in myself. She welcomed me into her lab despite the fact I did not believe I had the experience I would need to succeed in bioengineering. She encouraged me to step outside of my comfort zone, think creatively, and to always ask questions.

There is no doubt about the valuable impact Olga Yakovenko has had on my experience. Olga has been a coffee buddy, an assay troubleshooter, a sympathetic ear, and a fellow fencing enthusiast. She has been a resource for scientific and life advice alike.

Next I'd like to acknowledge my fellow Thomas lab grad students. Molly Mollica is an incredible person with focus, motivation, and organizational skills rivaled by few. Molly is a wonderful person to work beside who inspires the people around her to be their best selves. Casey Kiyohara, a fellow snack-enthusiast, has been stumbling through grad school with me. Casey has commiserated with me countless times over the difficulties of long meetings with Wendy, troubleshooting binding assays, and wondering what is wrong with the autoclave. Casey has an uncanny ability to spot every typo on my power point slides and has proofread numerous documents and emails for me.

The Thomas lab tends to attract some amazing undergraduate students. In particular, I'd like to thank Lesley Martinez Rodriguez, with whom I have spent countless hours discussing books shows, songs, and memes. Although Amy Stegmann left the Thomas lab to begin her graduate career not long after I joined, I have been blessed by her friendship throughout my time at UW and

her insistence on Friday board game nights that motivated me to leave lab at a reasonable hour on Fridays.

Next, I'd like to thank the incredible FimH group of the Sokurenko lab, Klevit lab, Stenkamp lab, and Interlandi lab. Our long and rigorous discussions not only helped me consider FimH beyond a bioengineering perspective, but also helped me gain the courage and confidence to speak up in a room full of individuals who are more knowledgeable and experienced than me. I must in particular acknowledge Dagmara Kisiela and Pearl Magala – the fellow scientists who collected the wet lab data that was often the subject of our FimH meetings. Dagmara and Pearl are two incredibly helpful and kind researchers who constantly went out of their way to help make my project just a little bit easier to tackle.

Next, I'd like to thank my wonderful friends I met in and outside of graduate school for all the times we had together. Spending time with them helped me get my mind off the latest problem in lab and take a break from research. Their humor and extensive baking sessions truly helped me get through the trying task of wrapping up my PhD in the middle of a pandemic.

I'd like to acknowledge the people at the Salle Auriol Fencing Club. The sport of fencing kept me sane throughout graduate school, but the support and friendships from my fellow fencers have made my experience unforgettable. I am also extremely fortunate in how my coach has encouraged me both on the fencing strip and on my academic journey.

Finally, I'd like to acknowledge my parents, whose influence has led me to become the person I am today. I am thankful that I have inherited their stubbornness that has helped me persevere through the challenges I encountered in graduate school.

Chapter 1. BACKGROUND

BIOLOGICAL ADHESION: SLIP, CATCH AND IDEAL BONDS UNDER FORCE

Forces can be found in nature as shear stress from high velocity fluids in the bloodstream or urinary tract, cell migration, saliva or tear formation, and intestinal peristalsis[1]. The application of force shifts the equilibrium of the breaking and forming of noncovalent bonds by lowering the free energy of the separation of the interaction[2]. The change in unbinding rate caused by force can be estimated by Bell's model[2]

$$k(f) = k^o e^{\frac{f\Delta x}{k_B T}} \quad (1)$$

where $k(f)$ is the modified rate constant, T is the temperature, k_B is Boltzmann's constant, f is the force applied, k^o is the dissociation constant in the absence of force, and Δx is the distance to the transition state. Often $k_BT/\Delta x$ is simplified as f_b and can be used to describe the force sensitivity of a system[3,4]. Noncovalent interactions that decrease in lifetime at a rate described by equation 1 are referred to as slip bonds. In slip bonds the value of Δx is positive (x>0) as force would cause $k(f)$ to be larger than k^o [5].

Catch bonds are a behavior reminiscent of a familiar gag toy: the finger-trap toy. The presence of force causes the bond to "catch", resulting in an overall increased bond lifetime[6]. A positive value of Δx is indicative of a catch bond[5]. The catch bond property observed in nature generally lasts up until a critical force, after which the interaction converts to a slip bond behavior[7,8].

Catch bonds are known to occur between many proteins and their ligands including cell adhesion molecules[9–12], motor proteins[13], and bacterial adhesive proteins[14,15]. Catch bonds serve as a means of regulated binding. In the bacterial adhesive, FimH, catch bonds allow for strong interactions in the presence of force and weak binding to ligands in solution that may serve as inhibitors[16–18], and facilitate cell spreading in biofilm formation[19]. L-selectins on neutrophils use catch bonds to decrease rolling velocity and facilitate cell attachments[12]. The catch bond formed when a T cell receptor binds a major histocompatibility complex serves as verification of attachment to the correct target and a signaling mechanism for activation of the T cell[20].

While the catch bond mechanism varies for each binding pair, it is generally believed to involve a change in the interaction between domains. Selectins have been proposed to have a sliding rebinding mechanism in which sufficient force causes an opening of the hinge angle between the two domains. In this new state, unbinding requires the ligand to slide across the binding surface, which increases the potential for rebinding[21]. One theory of the mechanism behind the cadherin catch bond involves a conformational change in a dimer pair that allows new contacts to form[22,23]. The serine-rich repeat adhesins found on *Streptococcus* allow the bacteria to infect heart valves by forming a catch bond with its binding partner to resist flow induced shear forces. It is suspected that under force, the domains of the adhesin rearrange to increase the number of contacts with the ligand[14]. Furthermore, in the *R. champanellensis* cellusome, which allows bacteria to adhere to plant fiber, the catch bond mechanism is believed to arise from unfolding of a regulatory domain[24]. The catch bond between *E. coli* FimH and mannose is believed to involve a force-activated allosteric change that increases the overall affinity of FimH for mannose[16,25,26].

In addition to slip and catch bonds, ideal bonds are a third form of force-characterized molecular interaction. Ideal bonds possess a force independent behavior. This behavior has only been observed during interactions between cadherins as a short lived intermediate state[9]. As a force pulls on a cadherin dimer, the cadherin molecules twist perpendicular to the direction of force, mitigating the effect of the force such that force does not affect the rate of unbinding[27].

FORCE SPECTROSCOPY TO MEASURE PHYSICAL PROPERTIES OF BONDS

Dynamic force spectroscopy and constant force for analysis of slip bonds

In addition to studying molecular bonds that are subjected to force in nature, force spectroscopy can also be a useful tool for characterizing the energy landscape associated with an interaction[3]. While the rate of a reaction is limited by the height of the energy barrier, mechanical force can speed up the reaction by pulling the molecule into a transition state as long as force is in the correct direction[3]. Force acts to lower the energy barrier to the transition state (Figure 1.1A) which increases the frequency of events and can significantly reduce long lifetimes[28]. Two common methods for probing the biophysical properties of a bond under force involve applying a linearly increasing force to an interaction until it ruptures and applying a constant force until the bond stochastically breaks.

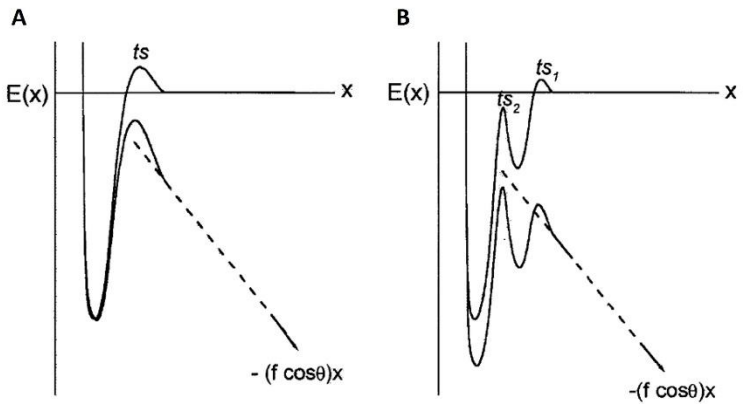

Figure 1.1. Force tilts the energy landscapes of an unbinding pathway, (A) lowering the energy barrier to the transition state (ts) and (B) exposing inner energy barriers that otherwise may have gone undetected. External force, f, at an angle, θ to the bond (location x) lowers the energy barrier by an amount equal to –(f*cosθ)x. From E. Evans 2001[3].

In dynamic force spectroscopy, a force opposing a molecular bond is increased at a constant rate, referred to as a loading rate, until the bond ruptures. The force reached at the time of rupture is noted and the rupture forces from hundreds of such experiments are combined in a histogram and the most frequent rupture force is noted as the rupture strength at this loading rate (Figure 1.2A) [3]. Rupture strength is typically measured at different loading rates, as the rupture force increases with the loading rate[3,28]. However, looking at how the rupture strength changes versus the log of the loading rate can grant insight into the properties of the bond. The slope of the linear relation observed when plotting the most common rupture force against log of the loading rate details the energy landscape associated with unbinding, and different slopes suggest multiple energy barriers (Figure 1.2B**)**[3]. Furthermore, extrapolation of this relationship can be used to estimate the force-free unbinding constant, k^o[3].

Force allows energy barriers that may not normally dominate the unbinding interaction to become prominent (Figure 1.1B) [3]. When measuring the strength of the biotin-streptavidin bond, for example, two distinct slopes were observed – one ranging over loading rates less than 10^4 pN/sec, and one at rates greater than 10^4 pN/sec (Figure 1.2B). These two slopes corresponded well with two transition states identified using molecular dynamics simulations[28].

Dynamic force spectroscopy though may not always capture a representative picture of unbinding kinetics. Dynamic force spectroscopy has failed to identify catch bonds that were later identified using constant force experiments[29]. Force could also remove an unbinding pathway that exists in solution and thus the impact of pathway would not be measured during a force assay. This would affect the estimated force-free dissociation rate, resulting in an estimated value of k^o that would differ from one that would be measured in solution[3].

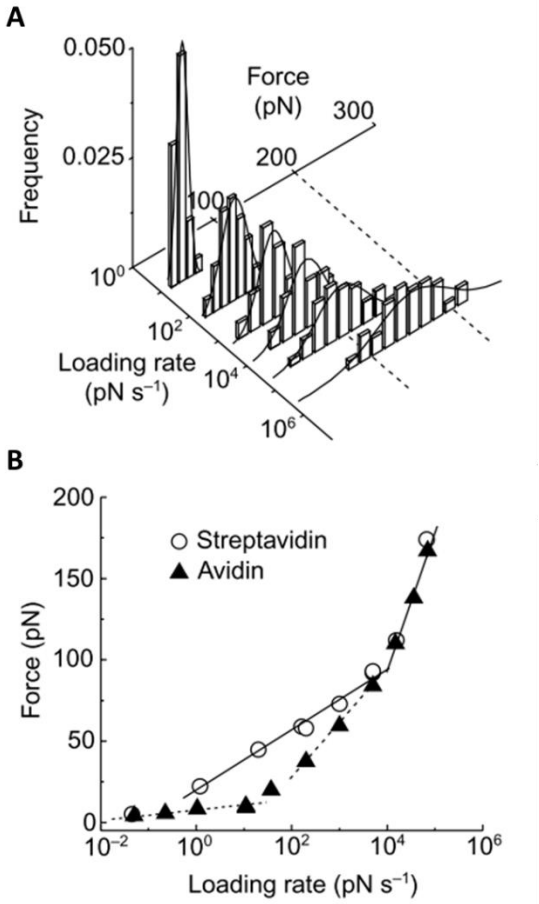

Figure 1.2. Influence of loading rate on rupture force in dynamic force spectroscopy. (A) Histograms of force at which biotin-streptavidin rupture under different loading rates. (B) Most common rupture forces for different loading rates reveal multiple energy barriers for the biotin-streptavidin and biotin-avidin bonds. From Merkel et al. 1999[28].

An alternative to dynamic force spectroscopy is constant force experiments, or force clamping, which can directly measure the lifetime of a bond under different forces[30]. In these experiments, the bond is subjected to constant force until it detaches. Often average lifetime over a span of forces is considered[30]. When the fraction of bonds surviving over time is plotted, an exponential decay behavior should arise that would linearize when the y-axis is on a log scale[11]. If the survival plot shows multi-exponential decay kinetics, this could be indicative of multiple unbinding states[7]. The rate of unbinding under force, $k(f)$ is estimated from $B(t) = B(0)e^{-k(f)t}$ [31] where $B(t)$ is bonds left at time, t. Equation 1 can then be fit to $k(f)$ over force to estimate the unbinding rate in the absence of force (k^o) along with the bond's force sensitivity (Δx).

Using force spectroscopy to measure catch bond strength

Another use of force spectroscopy is to identify the catch bond behavior of molecules. As catch bonds turn into a slip bond at high forces, unbinding typically involves more than one unbinding pathway[8] that can be measured with force spectroscopy. When applying a linearly increasing force to a catch bond, two distinct force peaks in the histogram of rupture forces are apparent at a large enough loading rate, which represent the two possible unbinding pathways. Changing the loading rate affects the presence of these force peaks. The second, higher force peak disappears at a low loading rate and the lower force peak disappeared at a higher loading rate[32,33].

Perhaps the more intuitive means of identifying a catch bond is to directly measure the lifetime of the interaction under a range of constant forces. Many catch bonds have been identified using constant force experiments[10,11,34].

Furthermore, force spectroscopy measurements have been used to understand the mechanism behind a catch bond. Under dynamic force spectroscopy P-selectins displayed the characteristic biphasic histogram of rupture forces. Evans et al. applied a nearly instantaneous increase in force before linearly increasing the force at a constant rate, which removed the low-force peak, suggesting that P-selectins can convert between the two unbinding pathways[32]. In another instance, the double exponential decay of the survival plot of bacteria adhesion in the flow chamber suggested the existence of a two-state catch bond[7]. Force spectroscopy has played a critical role in identifying and characterizing the behavior of bonds under force and the mechanisms behind molecular interactions.

THE FIMH CATCH BOND

Role of fimbria and FimH in bacterial adhesion

E.coli express long organelles that facilitate bacterial attachments in high shear environments (Figure 1.3). The fimbriae, also known as pili, are each composed of a long coiled chain of proteins capable of uncoiling in the presence of applied force (Figure 1.3B) [35]. While *E. coli* are known to express multiple types of fimbria, type 1 is the most common[36]. Type 1 fimbria contain thousands of copies of the protein FimA, and one each of FimF, FimG, and FimH. These three terminal proteins compose what is known as the fimbrial tip. The individual proteins are stabilized together by a donated β-strand integrated into the β-sheet of a succeeding protein[37]. While the proteins themselves are rather rigid, there is a great deal of flexibility at the interface of the proteins[38]. This flexibility is believed to allow the fimbriae to easily explore areas for available mannose sugars.

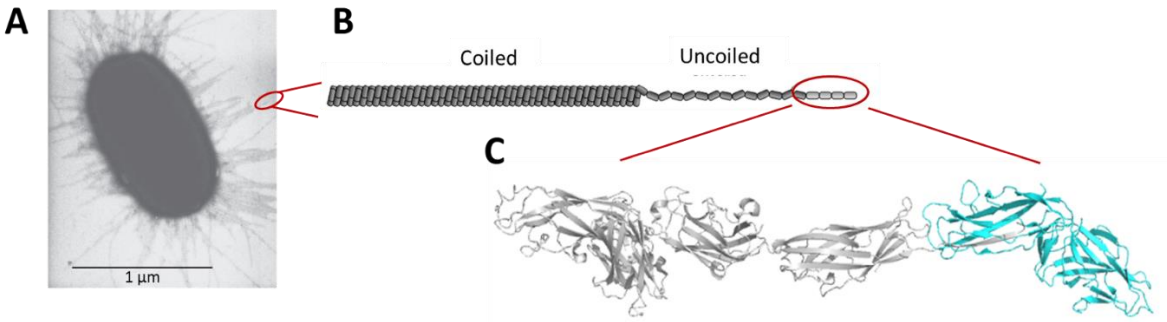

Figure 1.3. FimH is located on the terminus of *E. coli* fimbria. (A) *E. coli* micrograph, adapted from Thomas, 2008[31]. (B) Diagram of fimbria composed of thousands of coiled copies of the protein FimA and the fimbrial tip (red oval), adapted from Whitfield and Thomas, 2011[39]. (C) Crystal structure of fimbrial tip. The terminal protein, FimH, is in blue. PDB: 3JWN.

The terminal fimbrial protein, FimH is a receptor protein that facilitates attachments in the presence of force and is highly conserved among *E. coli* (Figure 1.3C)[38]. *E. coli* are the most common cause of urinary tract infections and FimH is believed to increase the virulence factor of these bacteria as the first step in infection is attachment to a host surface[40,41]. FimH recognizes and forms catch bonds with the sugar mannose, which is typically found as glycosylations on glycoproteins. The catch bond property of FimH allows *E. coli* to bind epithelial cells in high shear environments, such as the urinary tract, and resist fluid-induced forces[15,42].

In addition to the FimH catch bond, the coiled fimbria regulate adhesion in the presence of opposing forces. At forces greater than 60 pN, the fimbria begins to uncoil, which serves as a buffer to absorb forces greater than 60 pN – the force at which the FimH catch bond is estimated to be longest lived[35]. Furthermore, uncoiling of the fimbria improves the flexibility of the structure[38] which could facilitate formation of contacts from additional fimbria on the bacterium.

The structure and conformations of FimH

FimH is composed of two domains, each of which is made primarily of β-sheets: a mannose-binding lectin domain and a regulatory pilin domain[37]. The lectin domain is an elongated β barrel-like structure which is connected to the pilin domain by a three-residue linker. The mannose binding pocket on the lectin domain is located distal from the pilin domain[37].

Interaction of these two domains acts as a form of allosteric regulation of the flexible mannose-binding pocket[43]. The pilin domain contacts the interdomain loops of the lectin domain (Figure 1.4A) which propagates a change through the lectin domain that leads all the way to the mannose binding pocket. The lectin domain of FimH has two distinct conformations from this regulation: a high-affinity state and a low-affinity state (Figure 1.4). When the pilin domain is not in contact with the lectin domain, the lectin domain is characterized by a closed binding pocket that increases mannose affinity by slowing the kinetics of association and dissociation. Contact with the pilin domain though, stabilizes a comparatively open binding pocket through an allosteric propagation that widens the β-barrel of the lectin domain[44]. This binding pocket conformation facilitates rapid mannose binding and unbinding.

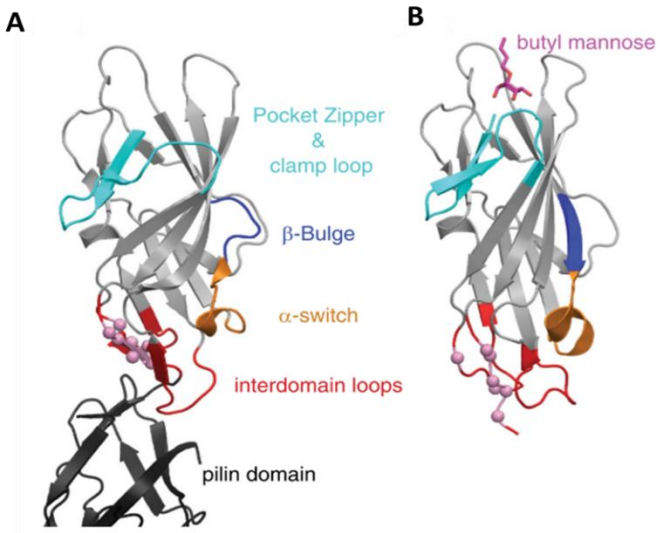

Figure 1.4. Regions of the FimH lectin domain involved in mannose binding and allosteric regulation. (A) Low-affinity state. (B) High-affinity state. From Rodriguez *et al.* 2013.

The presence of the pilin domain is essential for stabilizing the low-affinity state. Weakening of the interaction between the pilin domain and the lectin domain, via either a mutation or an antibody, induces the same high-affinity state as force. In addition, the lectin domain, when expressed without the pilin domain, is primarily in the high-affinity conformation. Since expression of FimH with additional proteins of the fimbrial tip encourages association of the two FimH domains, FimH is preferentially in the low-affinity state in the absence of force[45].

The transition from the low-affinity state to the high-affinity state occurs via an intermediate conformation. This intermediate, originally proposed in Rodriguez et al.[46] and later crystallized in Sauer et al.[25], consists of the general compressed shape of the low-affinity state but the closed binding pocket of the high-affinity state. Binding of mannose to the low-affinity state induces the closing of the binding pocket[25]. If a force is applied to this state which pulls the pilin domain away from the lectin domain, the high-affinity state of FimH bound to mannose is stabilized[26,45].

The structures of the binding pocket when FimH is in the high-affinity and low-affinity state and the hydrogen bonds mannose forms with residues in this pocket were explored using molecular dynamics and steered molecular dynamics simulations[47]. Normally mannose rests in the binding pocket parallel to the floor of the pocket (Figure 1.5A). This position maximizes the number of hydrogen bonds the sugar can form with FimH. However, an alternative, mannose orientation was identified in which mannose flips 90° into a perpendicular position – essentially standing up in the binding pocket. In this position, mannose is not stabilized by as many hydrogen bonds and thus forms a weaker interaction with FimH (Figure 1.5B)[47]. Under excessive force, the catch bond property of FimH no longer mitigates force and FimH take on a slip bond behavior. It is suspected that this perpendicular mannose position represents the pathway through which mannose unbinds from the high-affinity state under excessive force and is characterized by a transition state distance (Δx from Equation 1) of 3Å[47].

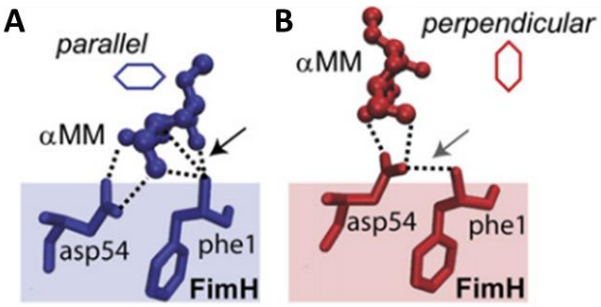

Figure 1.5. Suspected orientations of mannose (αMM) in the binding pocket (A) Parallel orientation (B) Perpendicular orientation. From Nilsson *et al.* 2008[48].

While the terminal mannose binds FimH in the binding pocket near the clamp loop, FimH residues outside the pocket can interact with structural moieties attached to the mannose residue. As a result, oligosaccharides and aglycones with terminal mannose sugars interact more strongly with FimH than single monomers of mannose. These additional structural moieties extending from mannose interact with the tyrosine gate (Ile52, Tyr48 and Tyr 137)[49,50]. Alkyl mannosides form hydrophobic interactions with the tyrosine gate that strengthen the ligand's interaction with FimH, with heptyl-mannose having the highest affinity interaction of the alkyl mannosides[50]. Oligosaccharides interact with the tyrosine gate through hydrophobic and aromatic interactions. The oligosaccharides with the highest affinity to FimH contain a Manα1,3Manβ1,4GlcNAc moiety[51], with the mannose adjacent to the terminal mannose interacting with Tyr48 and the GlcNAc interacting with Tyr137[52,53].

FimH variants and mannose affinities

Different strains of *E. coli* tend to have different variants of FimH with different mannose affinities[54,55]. Some variants have sequence differences of only a few amino acids or even a single base pair despite having vastly different affinities. Variants that tend to have a lower overall affinity for mannose tend to be found in the intestinal tract whereas higher affinity variants are from uropathogenic strains of *E. coli*[55].

Mutations in the pilin domain that affect association between the lectin and pilin domain have been found to increase favorability of the high-affinity state in FimH. The receptor protein, FocH, has 36% sequence homology to FimH and an extremely high affinity for its ligand[54]. Replacement of 17 residues of the pilin domain with the corresponding residues of FocH cause FimH to lose its catch bond property and remain stabilized in the high-affinity state[26,43]. One of these mutations, A188D, was found to be responsible in large part for the shift to the high-affinity state. This mutation alone is found to increase the favorability of the high-affinity state, although not as strongly as the FocH mutation[43], by weakening the association between the lectin and pilin domains.

Use of force spectroscopy to characterize FimH binding properties

The mechanism of FimH adhesion to mannose has been extensively studied by force spectroscopy techniques. An initial study found early evidence of the FimH catch bond by exploring how a mixture of guinea pig red blood cells (RBCs) - a common model target for binding of type 1 fimbria – and FimH-expressing bacteria clumped in the presence of dynamic rocking but did not clump in static conditions[15]. Further studies utilized a flow chamber to measure the adhesion of bacteria to an RBC-coated surface in the presence of shear forces. Researchers found that RBCs adhered to the bacterial cells at moderate shear but not low or high shear in a reversible manner[15].

When *E. coli* containing FimH were flowed over a mannose-coated surface in a flow chamber, the bacteria displayed a ‘stick and roll’ behavior, in which the bacteria appeared to either stick or roll across the mannose-coated surface depending on the magnitude of the shear[56]. At medium shear new bonds form as old bonds stochastically break, causing the bacteria to roll over a surface. At high shear, the increased force activates FimH into its high-affinity state, causing the bonds to be longer lived and the bacteria to ‘stick’ to the surface[56]. It was later confirmed through

simulations that the rolling behavior was due to the formation of new fimbrial contacts as FimH in the low-affinity state dissociated from the mannose-coated surface. Shear encouraged FimH rotation, which facilitated new contacts. The 'stuck' bacteria observed at high shear though were the result of the FimH catch bond[57].

To estimate the binding kinetics of bacteria to a mannosylated surface, the time a bacteria stuck or paused on the surface was measured at different shear rates in the flow chamber. The plot of fraction of pauses that survived over time exhibited a double exponential decay at all shear strengths analyzed[7]. Based on this behavior, Thomas et al. hypothesized that FimH possessed two conformations with strong and weak affinity for mannose that FimH interconverted slowly between, relative to the data collection rate[7]. The proposed model to describe this trend was shown to be capable of explaining the double exponential decay trend[7] unlike simpler, previously proposed models[7,8].

This catch bond model was further confirmed using single molecule dynamic force spectroscopy by AFM. The histogram of rupture forces at a single loading rate exhibited a bimodal distribution, which is characteristic of catch bond behavior[26,32]. Furthermore pre-activating FimH before applying a linearly increasing force, either by a mutation, antibody, or preloading force, resulted in just a single peak in the histogram of rupture forces[26], as observed in other catch bonds[32]. Pre-activated FimH displayed a similar maximum rupture force as untreated FimH[16,26]. These pretreatments encouraged the high-affinity state and demonstrated that FimH could convert between the low-affinity state to the high-affinity state and that the two states were not separate poopulations[26].

FimH not only plays a crucial role in bacterial adhesion, but also is an interesting model for catch bonds and force-regulated adhesion. FimH's two-domain structure is relatively simple, which led to an early understanding of its catch bond mechanism. Despite extensive studies to understand the force-induced conversion between FimH's two states, the lifetime of FimH under force has not been well characterized. Measurement of this lifetime will help us better understand the difference in binding strength of the two conformations and the extent to which force increases the lifetime of FimH.

Chapter 2. MODIFICATION TO AXIAL TRACKING FOR MOBILE MAGNETIC MICROSPHERES

Laura A Carlucci and Wendy E Thomas

This is a working manuscript that has been submitted for publication.

ABSTRACT

Three-dimensional particle tracking is a routine experimental procedure for various biophysical applications including magnetic tweezers. A common method for tracking the axial position of particles involves the analysis of diffraction rings whose pattern depends sensitively on the axial position of the bead relative to the focal plane. To infer the axial position, the observed rings are compared with reference images of a bead at known axial positions. Often the precision or accuracy of these algorithms is measured on immobilized beads over a limited axial range, while many experiments are performed using freely mobile beads. This inconsistency raises the possibility of incorrect estimates of experimental uncertainty. By manipulating magnetic beads in a bidirectional magnetic tweezer setup, we evaluated the error associated with tracking mobile magnetic beads and found that the error of tracking a moving magnetic bead increases by almost an order of magnitude compared to the error of tracking a stationary bead. We found that this additional error can be ameliorated by excluding the center-most region of the diffraction ring pattern from tracking analysis. Evaluation of the limitations of a tracking algorithm is essential for understanding the error associated with a measurement. These findings promise to bring increased resolution to three-dimensional bead tracking of magnetic microspheres.

INTRODUCTION

Three-dimensional tracking of microspheres (often simply called beads) is useful in various biological fields to study processes as diverse as bacterial motion[58], opening and closing of a DNA hairpin[59], protein unfolding[60], and chromosomal motion[61], and plays an important role in various

biophysical techniques including optical trap[62], centrifugal force spectroscopy[63], and traction force microscopy[64]. Bead tracking in the z- or axial direction (perpendicular to the focal plane) is particularly important for magnetic tweezer usage[65]. Magnetic tweezers apply forces on molecular interactions through the usage of magnetic beads and magnets. In many magnetic tweezer experiments, the movements of the magnetic beads are monitored through the objective of an inverted microscope and recorded with a high-speed camera. Magnetic beads have high variability in magnetism and thus force must be calibrated for each individual bead[66]. The movement of the magnetic bead along the axial direction can be used to calculate the force on a bead and therefore on the molecules attached to the bead[67,68].

Although many methods provide robust sub-pixel resolution of lateral positions[69,70], tracking in the axial direction requires a different approach with unique challenges. Optical tweezers utilize quadrant-photodiode tracking in which the 3D position of a trapped particle is estimated from laser light scattered off the bead[69]. However, this method can only track one bead at a time. In contrast, two camera-based tracking techniques[63,71] can determine the z-positions of multiple beads simultaneously. One technique uses holographic tracking microscopy and Mie scattering theory. Holographic images are generated from light scattered by a particle and fit with the Lorenz-Mie scattering theory to estimate the distance the particle is from the focal plane with nanometer resolution[72]. Another common technique involves utilizing a Look Up Table (LUT) of off-focus images generated by moving a microscope objective or piezo stage and taking images of a bead at evenly spaced intervals over an axial range. The pattern of diffraction rings around the off-focus bead is used to generate a radial profile for each bead which corresponds to a known distance from the objective. The radial profile of a bead at an unknown position is compared to the LUT and inter-step z-position is inferred via interpolation of the steps in the LUT[71].

Although in principle each of these methods can provide up to sub-nanometer-level resolution[63,73], several factors affect the accuracy of tracking moving beads in the axial direction. First, it has been previously demonstrated that low nanometer-level precision only occurs within a narrow region near the focal plane[71,74,75]. Many 3D bead tracking methods typically explore a range of no more than 20 μm[71]. The accuracy of tracking varies greatly even within this range and the optimal axial range spans just a few microns[71]. A distance of a few microns is sufficient when estimating the unfolding of proteins[60,76,77]. However this distance is insufficient when using long linkers such as bacterial fimbria[35] or long DNA[78], or when tracking large movements of an

untethered bead[35,67]. For applications that require tracking a magnetic bead over tens of microns, overall tracking accuracy decreases.

A second potential mechanism for generating tracking errors is that a bead may move during acquisition of a single image, leading to blurring of the bead. In theory, movement within the lateral plane or in the axial direction might distort the radial profile.

A third mechanism for the loss of tracking precision involves the non-uniformity of the beads themselves contributing to poor tracking accuracy. Bead imperfections are known to interfere with holographic tracking due to their inability to fit Lorenz-Mie scattering theory well[74]. LUT tracking utilizes reference images, typically taken from the same bead of interest while not moving. It has been shown that the polydispersity of beads results in significantly higher error when the LUT is generated from a different bead compared to the same bead of interest[79]. As an asymmetric bead rotates, the diffraction pattern of the bead may be as dissimilar to the originally viewed pattern as that of a different bead. These concerns raise the question of whether the precision of the LUT method would also be sensitive to focal distance, bead blurring, or rotation of non-uniform mobile beads.

The impact of bead movement is not addressed by common methods of calibrating the accuracy or precision of a tracking algorithm, including using simulated bead images with added noise[70,75,80,81], tracking a bead that is non-specifically adsorbed onto a surface when the microscope stage is stationary[59,82,83] or moving[59,71,74], or tracking the z-positions of a tethered magnetic bead held taut under a magnetic field[75]. It therefore remains necessary to evaluate to what degree bead movement contributes to error in LUT tracking algorithms.

In this work, we explore the precision of tracking of freely moving beads over an axial distance of almost 100 μm, compared to stuck beads, for a tracking method based on the algorithm described by Van Loenhout et al.[73] that utilizes quadrant interpolation and a LUT. As expected, we found that the combination of free movement of a bead, along with the larger tracking distance, resulted in a relatively large standard deviation of estimated positions compared to immobilized beads. We also test and optimize modifications in the tracking algorithm that reduce the impact of bead mobility. We found that part of the error associated with mobile beads could be rectified by excluding pixels corresponding to the center of the bead when evaluating the z-position from the LUT. These modifications will greatly increase the precision of tracking and improve the estimation of the error of the tracking algorithm of a freely moving bead over a large axial distance.

METHODS

Chamber construction

Chambers were constructed as described in Johnson et al. 2017. Briefly, chamber slides (Fisherbrand Microscope Cover Glass, 24 x 60 x 1.5, Fisher Scientific) were rinsed with 70% ethanol and dried. Chambers were assembled with double sided sticky tape and injected with approximately 80 μL of 0.2% PBS-BSA (Sigma, Cat # A3059). Chambers were covered and stored overnight at 4°C.

Magnetic microbeads

Magnetic beads were diluted 100- fold in 0.2% PBS-BSA. Unless specified the magnetic beads used were 8.3 μm diameter (Compel Magnetic Microspheres COOH modified, Bangs Laboratories Inc., Cat# UMC4001). Other beads used were 2.8 μm diameter (Dynabeads M-280 Streptavidin, Thermo Fisher Scientific Cat# 11205D), 5.8 μm diameter (Streptavidin Coated Compel Magnetic Microspheres, Bangs Laboratories Inc., Cat# UMC0101), 8.8 μm diameter (Carboxyl Magnetic Particles, Spherotech Cat# CM-80-10), 11.0 μm diameter (Carboxyl Magnetic Particles, Spherotech Cat# CM-100-10).

Chambers with Immobilized Beads

Beads were nonspecifically bound to a slide by adding 100 μL of beads diluted 100-fold in water in the center of a cleaned slide. The slide was heated at 37°C until all liquid evaporated. Slides were rinsed with PBS and chamber was constructed as described above.

Magnetic Tweezer usage

A magnetic tweezers with bidirectional force control was used as described in Johnson et al.[67] with a 0.45 NA 20x objective installed (Figure 2.1A).At the start of each run, 20 μL of diluted beads are injected into the chamber and allowed to settle. The upper magnets were turned on with a voltage of 40 V and 0.1 amps for one second, after which the lower magnets were turned on with 40 V and 5 amps for 4 seconds. The upper and lower magnets were alternately turned on 2 more times each at the same current and voltage. One second separated the switch between each set of

magnets to ensure both magnets were never on simultaneously. Bead images were recorded at 18 frames-per-second.

Because the 5.8 and 2.8 μm beads are lower in mass than the larger beads and move slower under the same magnetic field, the lower magnets remained on for a total of 6 seconds to ensure the majority of beads encountered the bottom surface and the frame rate was reduced to 15 frames per second.

Immobilized beads were tracked at 18 frames per second for a total of 4 seconds while the beads were on the chamber floor. The chamber was then flipped upside down so that the immobilized beads were on the chamber surface and the beads were tracked in the same way as when they were on the floor.

Bead Tracking

Lateral bead tracking

Beads were tracked with a method based on quadrant interpolation from Van Loenhout et al[73]. In short, using a custom MATLAB script[84] (MathWorks, Natick, MA) initial estimates of the coordinates of a bead are input by the user. A square cutout of the image is taken surrounding the input coordinates. The image cutout is then rotated 90° and the fast Fourier transform of both the original and rotated images are taken. The pixel shift needed to align the Fourier transform of both images is used to estimate by how many pixels the input coordinates are off from the true bead center. Subsequent images are calculated as thus, using the calculated bead center from the previous frame as the starting coordinates as the initial guess of the bead centroid.

Axial bead tracking

Tracking along the z-axis is based upon Zhang et al., Van Loenhout et al., and Johnson et al.[67,71,73]. As the beads move in and out of focus the diffraction ring patterns around the beads change. This pattern is compared to the diffraction ring patterns of calibration beads by reducing the grey-scale bead image to a radial profile. Bead images are background subtracted to account for gradients in light. Radii are drawn from the center of the bead (as calculated in the above section) evenly spaced around a bead. The pixel intensities at each position along these radii are calculated and averaged together to create a single radial profile for each frame for each bead (Figure 2.1B). As the bead images are background subtracted, pixels darker than the background

have a negative intensity. These radial profiles are compared to a LUT, generated in a similar manner using calibration images. To minimize error associated with bead-to-bead variation, each LUT is customized to be the average of the radial profiles of 5 calibration beads that most closely match the analysis bead, further described below. Z-positions of a bead in each frame are estimated by finding the radial profile in the averaged LUT stack with the lowest root mean square error (RMSE). To obtain a resolution smaller than the step size of the LUT, the radial profiles are interpolated using a cubic-spline.

LUT generation

A z-stack of a field of calibration beads is collected with images taken at a range starting from an approximate 'in-focus' plane and ending 200 μm below this focus at 2 μm intervals for a total of 100 images. Each bead in the field of view is processed to create a separate LUT. Upon analysis of the first frame of an analysis bead in a video, the analysis bead is compared to the LUT of each calibration bead to find the closest matching radial profile. The root mean square error between the closest radial profile of each calibration bead and the radial profile of the analysis bead is calculated. The five calibration beads with the lowest associated error are identified as the ones most similar to the analysis bead. The radial profiles of these LUT are averaged together for each 2 μm step to generate a composite LUT that is used to calculate axial position of the analysis bead. Using this averaging approach reduces bead-to-bead variability and ensures one calibration bead is not biasing the analysis method. A new averaged reference stack is generated for each analysis bead and used to track the bead through the entire video from the array of LUTs. A different field of calibration beads is collected for beads of each size but the same field of calibration beads is used for all beads of the same size analyzed in this work.

Estimation of chamber floor and ceiling

Due to variations in the magnetism of the beads, each bead moves with a different velocity and thus takes different amounts of time to traverse the chamber and reach the opposite surface. The first frame in which a bead reached the surface was estimated as either when the difference between two consecutive axial positions was the opposite sign as the immediately preceding difference in positions or when the magnitude of the next five changes in axial position were each

below 250 nm. The moment the bead leaves a surface can be determined from the time the opposing magnetic field is switched on.

Estimation of bead velocity

Bead velocities are estimated by identifying z-positions that fall within the middle third region of the chamber. A linear regression is fit to these points and the velocity is taken from the slope. The fractional σ of the velocity is found by dividing the standard deviation of the three velocity measurements by the average velocity.

Statistical analysis

Confidence intervals were determined by and all statistical analysis was performed using GraphPad Prism 9 (San Diego, CA). As the distribution of errors is not normal, nonparametric tests were used. When comparing immobilized to mobile beads (in Figure 2) the Kruskal-Wallis test, followed by Dunn's multiple comparison test was used. A total of 90 immobilized beads on the floor over 10 videos and 79 immobilized on the ceiling over another 10 videos were collected in one day. These were compared to mobile 8.3 μm beads.

When comparing the various analysis methods, pairwise analyses were performed as the data sets were generated from the same beads. When comparing three or more data sets (as in Figure 2.4), a Friedman test was first used to identify whether there was any difference in the groups, followed by Dunn's multiple comparison test to determine how each method compared to the others. When comparing just two data sets (as in Figure 2.5), the Wilcoxon signed rank test was used. Only beads that stayed in the field of view and thus could be tracked through three successive up/down pulls were kept, resulting in a total of 223 beads across 44 videos collected on three separate days for the 8.3 μm beads. 151 2.8 μm beads across 12 videos in one day were collected. 89 5.8 μm, 136 8.8 μm, and 93 11 μm beads were collected across 15 videos each in one day.

RESULTS

To measure the precision of our tracking algorithm on a dynamic bead, magnetic beads were manipulated in a bidirectional magnetic tweezer set up (Figure 2.1A). Magnetic 8.3 μm diameter beads (Bangs Laboratories) were tracked in the z-axis by reducing the pattern of diffraction rings

around the bead to a radial profile, which was compared to a LUT of similar profiles collected from calibration beads at known axial positions (Figure 2.1B). To increase throughput, a single field of view containing 27 reference beads was used to create a collection of LUTs to calculate axial positions for all beads of the same size. To minimize error due to the bead-to-bead variation, each bead was analyzed using a composite LUT made up of the 5 reference beads most similar to that experimental bead.

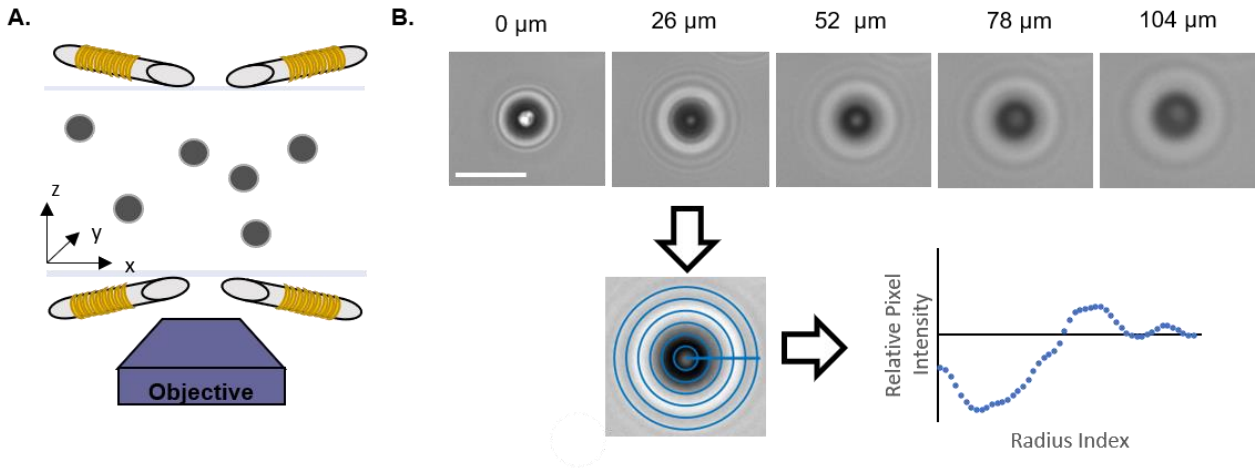

Figure 2.1. (A) Illustration of a magnetic tweezers with electromagnets. Magnetic beads (gray circles) are manipulated by electromagnets positioned above and below a chamber. A microscope objective views the beads from below the chamber. (B) View of magnetic beads from the microscope objective with beads at different distances below a relative focal point. Scale bar = 20 µm (73 pixels). Radial profiles are generated by radial projection in which pixels evenly spaced from the center are averaged together.

To assess tracking error in the absence of bead movement, we first measured the precision of the tracking algorithm with beads immobilized on the chamber ceiling or floor. The standard deviation (σ) of all positions for a bead reflects the precision. With the beads on the floor, the σ was found to be 0.1 µm. As expected, the precision decreased when the beads were on the ceiling, to a σ of 0.25 µm.

A field of beads was exposed to 3 successive rounds of repeated up/down pulls with one second pauses between each pull. Beads were pulled up with a force stronger than the force pulling them down. An axial position vs time graph of a bead gives some indication about the quality of a bead track. We would expect the bead to appear to alternate between the chamber ceiling and floor with distinct ‘flat’ regions in which the bead stops moving. The ‘flat’ regions corresponding with the floor or ceiling should be in approximately the same z-location as the bead returns to the same

surface after each pull. We noticed great variability in how well certain beads were tracked using this method. Some axial position vs time graphs show the bead moving as expected (Figure 2.2A). However, the axial position vs time graphs of other beads had obvious artifacts, such as inconsistencies in the location of the ceiling or fluctuations in the location of the ceiling or floor (Figure 2.2B). The fluctuations in positions at the floor at frames 80 and 232 were associated with rolling of the bead across the chamber floor in the lateral direction due to the slightly asymmetric magnetic field. At frame 232 the bead appears to rotate, which coincides with the bottom magnets turning off. The axial positions of the surfaces should be fairly consistent across the chamber, and no irregularities are observed on the chamber floor or ceiling that could explain the observed jumps in axial position. These observations suggest that rotation combined with lateral movement of the beads in relation to the objective, may result in the observed tracking errors.

We next quantified the precision of tracking mobile beads. We refer to each time the bead remains on one of the surfaces as a dwell. Each dwell lasted at least one full second (or 18 frames) but often longer, depending on the time needed for the bead to traverse the length of the chamber. To estimate the precision for tracking a bead held against a surface by a magnetic field, we calculated the standard deviation of all axial positions for the timepoints of each dwell. Unlike immobilized beads, beads held to a surface by a magnetic field are free to rotate or move laterally. These precisions decreased significantly ($p<0.0001$, as determined by Kruskal-Wallis test), compared to the corresponding values of immobilized beads, with a within-dwell σ of 0.52 μm and 0.80 μm for beads on the floor and ceiling respectively (Figure 2.2C).

We also looked at the precision of bead tracking as the bead leaves and returns to the floor and ceiling by taking advantage of the successive up/down motion of the beads. In this assay, each bead dwelled on the ceiling and floor three times each. The positions of each dwell were averaged together to obtain three values for the ceiling, and three for the floor. The standard deviation of the three floor and ceiling values reflects this between-dwells precision and were 0.9 and 2.6 μm (Figure 2.2C). These values were significantly different ($p <0.0001$) from each other and the corresponding within dwell standard deviations.

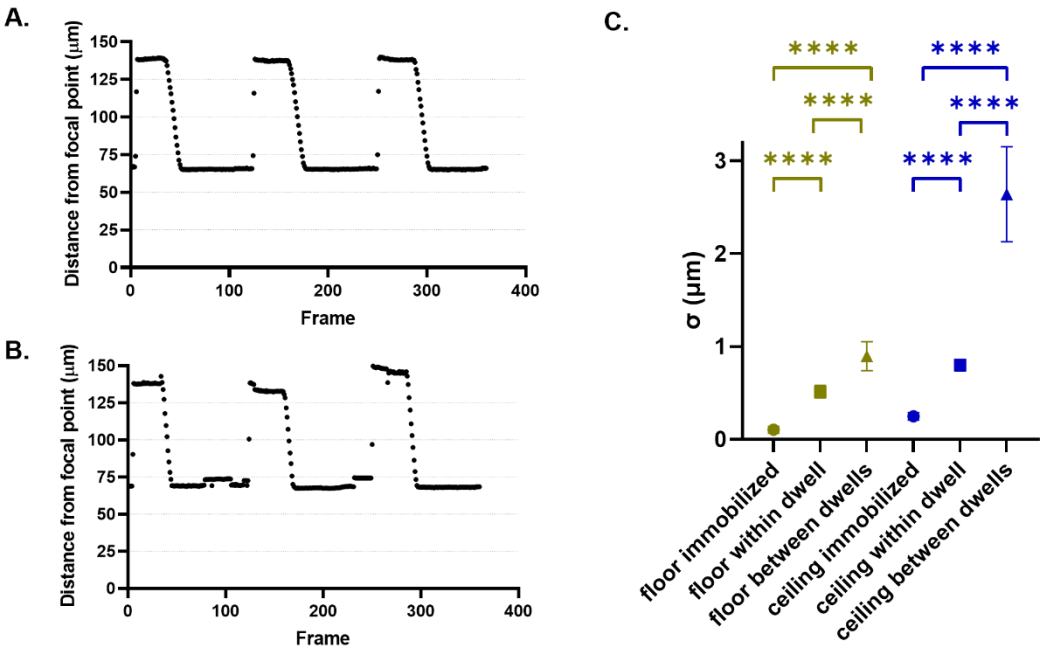

Figure 2.2. To characterize the accuracy of the tracking method beads were successively pulled to the top and bottom of the chamber (A) Example of an ideal trace where the bead stops moving at consistent z-positions, indicating consistent estimation of the ceiling and floor of the chamber. (B) Example of a clearly erroneous trace in which the positions of the chamber ceiling and floor are inconsistent. (C) σ of positions on the floor and ceiling when beads were immobilized, σ of positions within each dwell, and σ of average position of dwells for each bead. Values indicate average σ and error bars indicate 95% confidence intervals. **** $p<0.0001$ as determined by Kruskal-Wallis test.

Radial profile modifications to improve bead tracking

Our tracking method utilizes radial profiles generated from the diffraction ring pattern around an off-focus bead image compared to a LUT of reference images to determine the axial position of a bead. We sought to determine if erroneous bead positions are the result of imperfections in the radial profiles. We identified bead traces with worse precision on the ceiling than the floor. An example trace is shown in Figure 2.3A which has a between-ceiling-dwell of 4.6 μm but only 0.34 μm for the floor. The within-dwell σ of ceiling positions for this bead ranged from 0.66 to 2.0 μm. The corresponding within-dwell σ of floor positions ranged from 0.18 to 0.41 μm.

All time points of the six surface dwells were identified (colored points in Figure 2.3A). The radial profiles from each of these time points were generated and overlaid (Figure 2.3B). Upon visual inspection we noticed that the overall shapes of the radial profiles lined up well for all beads

on the same surface. However, the profiles had discrepancies in the maximum and minimum pixel intensities, and these discrepancies were larger for the ceiling than for the floor profiles.

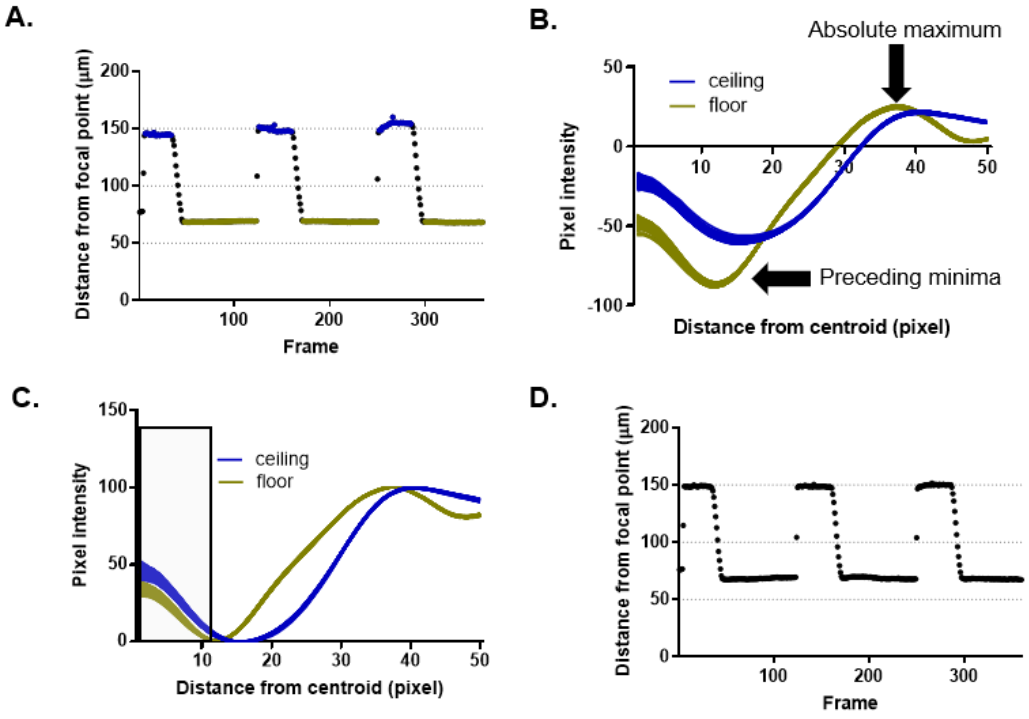

Figure 2.3. Modifications to radial profiles can remedy apparent tracking inaccuracies. (A) z-position vs frame plot of example bead exhibiting varying ceiling estimation. Colored points indicate when bead was identified to be on a chamber surface (B). Overlay of radial profiles of bead from (A) when on the chamber ceiling and floor. Regions where the overlay is thicker indicates higher variability between radial profiles. Black arrows indicate extrema of profile shape used to estimate region of truncation (see text). (C) Overlay of radial profiles from (B) after radial vectors have been scaled. Greyed box indicates region of radial profile truncated from z-position analysis. (D) z-positions of bead from (A) after all radial profiles have been scaled and truncated.

We hypothesized that pixels with the lowest and highest pixel intensities occurred the same distance from the bead center, and the only variation was the magnitude of the intensity of the maxima and minima. Therefore, all radial profiles were scaled so that the pixel intensities ranged from 0 to 100. A similar process of normalizing the radius vector has been implemented in other works for tracking beads in the z-axis to accommodate for variations in illumination[79,85].The radial profiles for each surface overlapped better overall but were still not completely aligned (Figure

2.3C). The pixels closest to the center of the bead still varied in pixel intensity. We truncated all pixels that were closer to the bead center than the earliest local minimum immediately preceding the absolute maximum, in all the radial profiles that correspond to the height region in which beads will be tracked (Figure 2.3B). For the 8.3 μm beads analyzed in this work, this was the first 11 pixels from the center. By truncating and scaling the radial profiles the new track of the same bead in Figure 3A had clearly more consistent ceiling positions. The within-dwell σ of ceiling positions ranged between 0.43 and 0.66 μm and the between-dwell σ of ceiling positions decreased from 2.6 to 0.62 μm (Figure 2.3D).

Modifying Radial Profiles Improves Surface Position Estimations

To characterize the effect of the radial profile modifications, we reanalyzed all bead tracks by (1) just scaling the radial profiles, (2) just truncating the radial profiles, and (3) both scaling and truncating. These modifications were only implemented to determine the axial positions and not the lateral. To evaluate the effect of modifying the radial profile, the changes in tracking precision were analyzed for the data set. The variation within ceiling and floor dwells were determined by looking at the σ of axial positions for all timepoints in a single dwell. The variation between dwells was found from the σ of the average position of each of the three dwells on the ceiling and floor.

All radial profile modifications significantly decreased the σ of positions within a ceiling dwell ($p<0.0001$) with truncating alone resulting in the largest decrease (Figure 2.4A). While the beads were on the floor, the σ of positions within dwells was significantly decreased by truncating alone or scaling with truncating the radial profiles ($p<0.0001$) (Figure 2.4A). These two modifications resulted in nearly similar average σ values.

When looking at the σ between dwells on the ceiling, the error also significantly decreased with all modifications, with the greatest effect being from scaling with truncating ($p<0.0001$) (Figure 2.4B). Scaling with truncating was not significantly different from truncating alone. No modification method generated a significant decrease of the σ between floor dwells (Figure 2.4B).

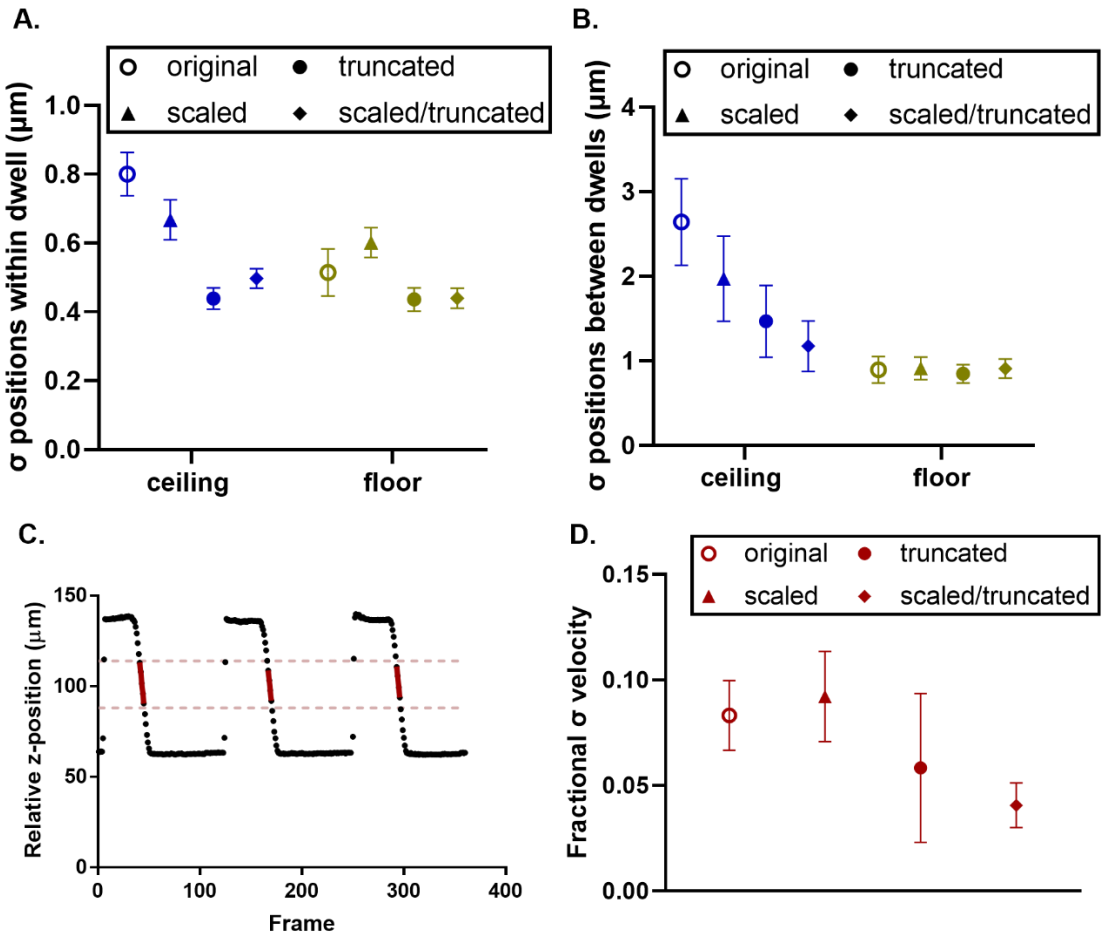

Figure 2.4. (A) σ of axial positions of ceiling and floor measurements within a single dwell. (B) σ of average ceiling and floor positions between 3 dwells. (C) The downward velocity of a bead moving through the middle of a chamber is calculated by fitting a linear regression to the bead positions as the bead travels through the middle third of the chamber. (D) The fractional σ, found by dividing the standard deviation of the three velocity measurements by the average velocity, is used to evaluate the precision of the velocity measurements. Values indicate average σ and error bars indicate 95% confidence intervals.

Variation in Bead Velocity

One routine purpose of bead tracking for magnetic tweezer use is to estimate the magnitude of the force being applied to a bead. This is frequently done on each bead because magnetic beads vary in magnetic properties and thus respond differently within a given magnetic field. To estimate the exact force applied to a bead, a modified version of Stoke's Law can be used to estimate force from maximum bead velocity while the beads are pulled by a magnetic field[67,78,86]. To characterize the precision of velocity measurements on moving beads, beads were pulled from the chamber

ceiling to the floor three times with identical magnetic fields with a force of approximately 5 pN. Any variation between the three velocities for each bead will be largely due to the analysis methods and is expected to scale with magnitude of the velocity. Therefore, comparison of the normalized error of the velocity measurements can serve as an additional form of error evaluation using axial positions between the chamber surfaces, which have not been considered so far. While we cannot easily compare specific axial positions beyond the chamber ceiling and floor, comparing the bead velocities measured during each pull on the same bead will also give us some insight in the precision of tracking in the middle of the chamber.

To find the velocity, the slope was calculated using a linear regression fit to the points that fall within the middle third of the chamber (Figure 2.4C). Beads near surfaces experience higher drags due to changes in fluid flow due to the presence of the surface but within the middle third of the chamber, the effects of the two surfaces are constant, so the standard approach for calibrating magnetic beads is to track in this region and use a correction factor[67,87]. To normalize the error so that the error of higher velocity beads does not dominate the measurement, we report the fractional standard deviation. The fractional standard deviation was calculated by dividing the standard deviation by the average of the three velocity measurements for each bead. (Figure 2.4D)

The average fractional standard deviation decreased from 0.083 to 0.040 upon scaling and truncating and to 0.058 when just truncating the radial profiles (Figure 2.4D), both of which indicate a statistically significant decrease ($p<0.001$). Scaling, either with or without truncating, did not provide a statistically significant improvement. Therefore, we conclude that truncating the radial profiles significantly improves measurement of bead velocity and thus the calibration of force applied by magnetic beads. Furthermore, it appears that truncation has a positive effect on the entire chamber and not just the chamber ceiling and floor.

Analysis improvements can be applied to different size beads

We next asked whether truncation was necessary due to some property that is unique to the 8.3 μm Bangs Laboratories magnetic beads we initially used or is more generally beneficial. We therefore collected additional tracks of moving beads, using beads of diameter 2.8 μm (Dynabeads), 5.8 μm (Bangs Laboratories), 8.8 μm (Spherotech), and 11.0 μm (Spherotech). These tracks were analyzed first without any radial profile modifications (original analysis) and then by truncation. For each bead type, the truncation point was determined to be the local minimum

immediately preceding the absolute maximum pixel intensity (Figure 2.3B), for the radial profiles obtained at the position closest to the focal plane (the chamber floor). The innermost 11 pixels were removed for the 5.8, 8.8 and 11 μm beads and the innermost 9 pixels for 2.8 μm beads.

For all bead sizes, truncation improved both within-dwell (Figure 2.5A) and between-dwell (Figure 2.5B) variation on the ceiling, and improved or had no significant effect on these variations on the floor. Interestingly, the smaller beads on the floor provided the most precise measurements of all conditions prior to truncation, but truncation was still immensely impactful for increasing precision of measurements on these small beads.

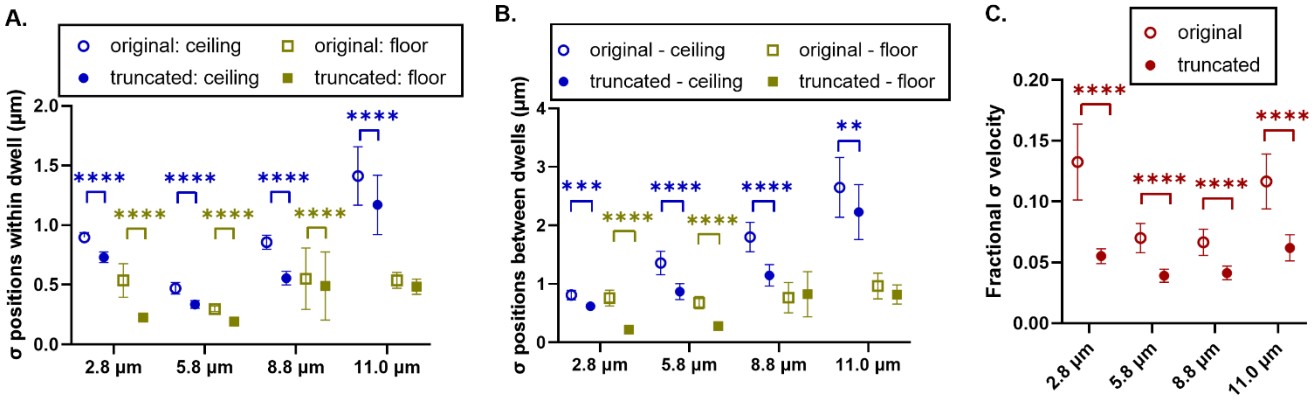

Figure 2.5. Improvement truncating radial profiles have on beads of various sizes. (A) σ of axial positions of ceiling and floor measurements within a dwell (B) σ of average ceiling and floor between 3 dwells (C) Fractional σ of velocity **p<0.01, ***p<0.001, ****p<0.0001 as determined by Wilcoxon signed rank test. Values indicate average σ and error bars indicate 95% confidence intervals.

Furthermore, for all beads analyzed, the velocity measurements were more consistent when the radial profiles were truncated. The change in the fractional standard deviation between truncating and not truncating is significant for all beads (Figure 2.5C). With the original analysis method, the fractional standard deviation ranges from 0.13 to 0.067 for the various bead sizes. Upon truncation of the radial profiles, this range reduces to between 0.062 and 0.037. This is noteworthy as measurement of bead velocity is commonly used to measure the force on magnetic bead in a magnetic field. Increasing the precision of velocity measurements therefore improves the estimation of force applied by magnetic beads.

In summary, truncation had marked benefits for measuring both position and velocity of all beads tested and did not exhibit a significant disadvantage in our assays. These results suggest

that truncation of radial profiles should be routinely implemented when tracking beads that are not immobilized.

DISCUSSION

Here we address errors that arise in tracking a moving magnetic microsphere by presenting a means to measure these errors and a simple method to minimize these errors. We observed that tracking errors of moving beads were significantly higher when the bead was farther away from the focal plane (Figure 2.2C) similar to what has been shown for immobilized beads in this work (Figure 2.2C) and in previous works[71]. However, we found that the error of tracking a moving bead was significantly higher than when tracking a stationary bead, even when nearer the focal distance. Using a high precision z-positioner to follow a moving bead could reduce the discrepancy in error observed at different axial positions, but such a positioner would not remove the error we observed when a bead was mobile compared to immobilized. Furthermore, a positioner is not practical in multiplexing applications in which beads are moving at different speeds, as was utilized here.

Blurring of the radial profiles could contribute to the tracking errors if the beads move significantly within the acquisition time of the camera. Beads are on average held to the bottom surface by 5 pN of force by gravity and the magnetic field in our assay. Using the formula for scale height to calculate H, the average distance from a surface of a particle subjected to thermal energy kT and a constant force F, we estimate that beads are expected to remain around a characteristic height of $H = \frac{kT}{F} = 0.8$ nm of the surface. While movement in the lateral plane may also reduce accuracy, we used a 5 ms acquisition time in this study, during which time an 8 um bead is expected to move less than 10 nm due to diffusion within the lateral plane[88,89], and even less due to the lateral velocities we measured. This is comparable to the precision of tracking the centroids of immobilized beads in the lateral plane. These calculations make it highly unlikely that blurring is a significant contributor to tracking error in our studies.

Moreover, the tracking errors did not appear as random fluctuations, but rather were highly correlated in time, with sudden changes in calculated axial position occurring occasionally as beads moved across a surface, the magnetic field changed, or when beads left and returned to the same surface. Artifacts caused by the movements of imperfect beads may also explain why some

beads have clearly visible artifacts in their tracking and other beads do not. We hypothesize that these errors occur as slightly irregular beads rotate, so irregularities affect the radial profiles in different ways. Presumably, tracking errors may be due to asymmetry in the bead images caused by the optical system. While this is possible in our system, these errors would affect both immobilized and mobile beads and thus would not explain the discrepancy in error between the two bead types.

For all bead sizes, these errors were significantly mitigated by truncating the radial profile to remove pixels closest to the center of the bead, especially in axial regions with the highest errors. We suspect truncating the radial profiles of a bead accommodates for imperfections in the bead geometry which result in highly variable pixel intensities in the center of an off-focus bead image. If a bead cannot rotate, these imperfections would not interfere with LUT comparisons and therefore, truncating the radial profile would not be necessary, and might even remove useful information for estimating the bead's axial position. This illustrates the importance of optimizing and characterizing tracking algorithms in a situation that addresses the full complexity inherent in the experimental condition in which the algorithm will be used.

We also tested whether scaling the radial profiles might help. If the poor tracking was due to sudden but subtle changes in ambient lighting or pixel acquisition time, then normalizing the radial profiles should help. In our case, truncation appeared to help slightly, but the improvement was rarely if ever statistically significant, whether applied to the original or truncated profiles. This suggests that irregularities in lighting or camera function were not significantly affecting our data. The value of scaling therefore remains unclear but may benefit other data sets and did not have a significant disadvantage in our hands.

It may be noted that our measured positions of immobilized beads still had a high standard deviation – over an order of magnitude larger than what was observed for immobilized beads in other works[73]. Because the errors caused by bead movement dwarf the errors in tracking immobilized beads, we do not find it effective to compromise efficiencies in our workflow to optimize tracking on immobilized beads, but it is worth explaining the source of these errors for others' consideration. A major limitation on precision of tracking immobilized beads in this work is the low magnification we used. It has been shown that the error associated with axial bead tracking increases as magnification and numerical aperture decreases[66], especially below 30x [73], and the publications reporting low nanometer resolution employed objectives with at least 40x

magnification[71,74,75]. Because we are interested in tracking relatively large microbeads (~8 um), we use a 20x objective to maximize the number of beads in a field of view. To further optimize our workflow, the same sample of calibration beads was used to create the LUT for all beads of the same size. In contrast, some studies take calibration images of each analysis bead before applying a magnetic field and use these images to calculate the axial positions of the same bead while moving[66,71,75]. Kovari et al. demonstrated that beads analyzed with a LUT generated from a different bead rather than the same bead decreased the tracking accuracy by over an order of magnitude, resulting in an error of 100-200 nm, comparable to what we observed[79]. An additional source of potential error is that we did not use an immobilized reference bead to subtract instrument drift[66,67], but instead use a perfect focus system to minimize drift to within 25 nm resolution (Nikon perfect focus system). While precision of immobilized beads could be optimized further, the improvement would be trivial compared to the large error contributed by the mobility of beads.

The modifications in LUT tracking methods we propose here should be broadly useful in biological measurements using magnetic tweezers because LUT is a common method used for 3-dimensional particle tracking due to its flexibility in microscope settings and low computational cost. Tracking of freely moving magnetic beads has been used to calibrate the force on a bead in a magnetic field from the viscous drag[68], measure the viscoelastic properties of cytoplasm[90,91], measure the mechanical properties of the nuclear envelope[92], and the inner cell mass of a mouse embryo[91]. Notably, while it may be possible to minimize rotational asymmetry through manufacturing processes, all types of beads we tested demonstrated significantly lower precisions when moving freely (Figure 2.5) than when immobilized[67], and all benefited from this modification of the tracking method (Figure 2.5). While we were unable to improve the precision to that of an immobilized bead, we found truncating the radial profiles significantly improved the tracking error in most aspects examined. Since truncating the radial profiles is a relatively easy process that does not add much computation time, we highly recommend this modification to be implemented when tracking moving beads.

Chapter 3. FIMH POSSESSES INCREDIBLY LONG LIFETIMES UNDER FORCE

Laura Carlucci and Wendy Thomas

This is a working manuscript that will be submitted for publication

ABSTRACT

To facilitate adhesion to host epithelial cells in the presence of a high shear fluid environment, FimH utilizes a catch bond behavior in which the lifetime of the bond with its ligand, mannose, increases with force. The mechanism of the FimH catch bond is known to involve a force-induced transition from a low-affinity state to a high-affinity state. However, the binding properties of the high-affinity state of FimH under force have not been fully characterized due to its unusually long lifetime even under force. To understand the strength of the high-affinity state, we measured its lifetimes using a constant force assay on a magnetic tweezer apparatus. We found that FimH unbound from mannose with multi-state kinetics. A double exponential decay fit identified two potential states with force-free unbinding constants differing by over an order of magnitude, but with nearly identical force sensitivity parameters. While one explanation for the multiple states could be the lack of true single-molecule measurements in our data set, the fit parameters cannot be explained by multiple bonds. We conclude that the measured behavior is the result of a heterogeneous FimH/mannose bond forming under force. While we remain unsure of the nature of these states, the lifetimes we measure suggest FimH is one of the longest-lived catch bonds in the literature.

INTRODUCTION

Fluid flow environments such as the mouth, the intestinal tract, and urinary tract generate strong shear forces that oppose bacterial attachment to the host[1]. Bacteria that colonize these environments must adhere to surfaces in the host despite these forces, to infect cells and form biofilms[41]. Most variants of uropathogenic and commensal strains of *Escherichia coli* express type

1 fimbria which end in an adhesive protein, FimH[40]. FimH contains two domains: a mannose-binding lectin domain, and a regulatory pilin domain that anchors FimH to the rest of the pili[37].

FimH resists strong shear forces in the intestinal and urinary tract by forming a catch bond with mannose[56], in which the lifetime of the interaction increases with increasing force[6]. This trend is only true up to a critical force threshold, after which, additional force weakens the interactions[33]. The mechanism of the FimH catch bond is associated with its different conformation states with distinct mannose affinities[25,26,93]. In the absence of force, FimH has a relatively low-mannose affinity. In this conformation the lectin domain has an open binding pocket and interacts with the pilin domain[93]. Upon initial mannose binding, the binding pocket tightens around mannose but the lectin domain is still in contact with the pilin domain[25]. Force induces FimH to enter a high-affinity state as the pilin domain is pulled away from the lectin domain and the lectin domain elongates, stabilizing the closed pocket[45,93]. This elongated state possesses a mannose affinity about three orders of magnitude larger than the low-affinity state[16]. The mechanism behind the catch bond behavior is the force-induced transition from a low-affinity state to a high-affinity state. When FimH can only populate the high-affinity state, such as by weakening the interaction between the pilin and lectin domain, the catch bond behavior disappear[26].

The strength of the FimH-mannose bond under force has been well-studied by force spectroscopy. Increased bacterial adhesion to a mannose-coated surface under shear conditions in a flow chamber was the first evidence of the bacteria's force-enhanced adhesion behavior and possible catch bond behavior[15,56]. The FimH catch bond was later confirmed by further flow-chamber experiments[56] and dynamic force spectroscopy in which an applied force is linearly increased over time[26]. While the binding kinetics associated with the catch bond have been estimated[26], the binding strength of the high-affinity state has not been fully characterized due to its incredibly long lifetime. The lifetime of FimH in the low-affinity state has been estimated to last less than 1 second[16]. The lifetime in the high-affinity state has never been fully measured, though initial studies found this lifetime to far exceed 20 seconds[45]. This conformation is important for *E. coli* adhesion in the presence of high shear forces. Therefore, measuring the lifetime of the high-affinity state of FimH under force can help us better understand the mechanism behind bacterial adhesion in flow.

While various instruments have been used to apply constant forces to bonds[30,60,94,95], most techniques rely on active feedback to regulate force[96] and thus are susceptible to errors for constant

force measurements. Alternatively, magnetic tweezers inherently work in a constant force mode as they use a magnetic field generated by either permanent or electromagnets to apply force to ligand-coated magnetic beads[97]. As long as the position of the permanent magnets or current of electromagnets remains constant, so does the force[97]. Magnetic tweezer setups have been demonstrated to be capable of applying constant forces for many hours[60]. Furthermore, magnetic tweezers sometimes have multiplexing capabilities that allow for the simultaneous measurements of long single-molecule lifetimes[60,98]. This would facilitate rapid collection of single molecule lifetime measurements.

Here we utilize a multiplexed magnetic tweezer to apply constant forces to the FimH-mannose bond to characterize the lifetime of the high-affinity state under force. We apply a preload force to all bonds before measuring the lifetime to induce the high-affinity state of FimH and confirm that we can reproduce the FimH catch bond behavior. We found that the lifetime of the high-affinity state bound to mannose was incredibly long-lived with many bonds outlasting the 15-minute collection period at forces up to 100 pN. In fact, when compared to other slip and catch bonds in the literature, FimH is extremely long-lived. The survival curves however, did not display the single exponential decay behavior expected, but rather fit a double exponential decay model. One common cause of this behavior is a high proportion of multiple bonds forming in the assay preventing us from measuring single-molecule kinetics. However, we used a dilute concentration of fimbria in which only 20% of beads form bonds with the surface, a common practice to ensure the majority of bonds are single molecule, based on Poisson statistics[99]. Furthermore, the parameters obtained from the double exponential decay fit could not be described by the formation of multiple bonds in our assay. Therefore, the double exponential decay behavior is likely the result of heterogeneity in the FimH-mannose bond.

METHODS

Slide and bead prep

8 μm magnetic beads (UMC4N Bang's Laboratories Inc. Fishers, IN) were prepared as described in Johnson et al[67] using mannan (M7504 Sigma) as the mannose-containing ligand and BSA as the negative control. KB91 fimbria were prepared as described in Tchesnokova et al[93]. Fimbria-containing chambers without reference beads were prepared as described in Johnson et al[67]. Briefly bottom coverslips, or chamber floors, were cleaned with acetone, ethanol, and water

before a drop of fimbria diluted to between 4 and 8 μg/mL was incubated on the surface. Top coverslips, or chamber ceilings, were cleaned with ethanol and chambers were assembled using one top and one bottom coverslip adhered using double sided sticky tape. Chambers containing immobilized reference beads were prepared in a similar manner, except a 100 μL drop of 6 μm polystyrene beads (Cat # 07312 Polysciences Inc, Warrington Pa) diluted 1:150 was placed on the center of bottom coverslip directly after cleaning. The slide was heated at 37°C until all liquid evaporated. Slides were rinsed with bicarbonate buffer before the drop of fimbria was incubated on the surface as described above.

Lifetimes collection

A bidirectional magnetic tweezer as described in Johnson et al[67], with a 0.45 NA 20x objective installed was utilized to apply forces to the FimH mannose bond. Slides were initially screened for an approximate mannan-bead adhesion rate of 20% or less and a BSA-bead adhesion rate of 1% or less by using the following magnetic tweezer protocol.

At the start of each run, 15-20 μL of beads diluted 10-fold in 0.2% PBS-BSA were injected into the chamber. The upper magnets were initially turned on with 40 V and 0.02-0.03 amps for 1 second to bring all beads to the top (non-fimbria coated) surface. Alternatively, in a minority of instances the chamber was flipped upside down so that beads would settle on the chamber ceiling before flipping right side up and placing in the magnetic tweezers. The bottom magnets were turned on at 40 V and 5 amps for 3 seconds, where the beads were pulled to the chamber floor and allowed to form bonds. The top magnets were turned on at 40 V and a current between 0.1 and 0.2 amps for the preload.

Lifetimes were collected beginning with the protocol used for screening. After the preload, the current was changed to between 0.02 and 0.2 amps and held constant for the next 15 minutes. One second separated the switch between each set of magnets to ensure both magnets were never on simultaneously. Beads were recorded at a sequence of framerate starting when the magnets initially turn on: 10 sec^{-1} for 200 frames, 1 sec^{-1} for 100 frames, and 0.1 sec^{-1} for 78 frames.

Analysis of Magnetic Tweezer Data

Positions of beads in three dimensions throughout the assay were determined as described in the previous chapter.

Force estimation

Due to the polydispersity of the magnetic properties of the beads, the applied force must be calculated for each bead[66]. A modified version of Stoke's Law ($F = 6\pi\mu vr\lambda$) is used to estimate the force on a bead based on its velocity[67,78,86,100], where F is the drag force, μ is the viscosity of buffer, v is the velocity of the bead, r is the radius of the bead, and λ is a correction factor due to the surface effects of the chamber[87]. As the framerate used is too slow to measure the velocity of a bead as it detaches from the surface (and some beads never detach during the collection period), the upward velocity of a bead under current used for the preload or lifetime measurement cannot be measured directly.

The ratio of the upward velocity and the downward velocity at set currents, is constant for all beads and is consistent across days. This ratio is determined for a range of currents, in a separate experiment by measuring the downward and upward velocity of many BSA-coated beads using the same voltage and currents used in the lifetime assay. In the lifetime assay, the downward velocity of the bead from before the bead contacts the chamber floor combined with the predetermined velocity ratios is used to estimate the upward velocity of the bead and thus the force applied to the bead. Downward velocities were calculated using a linear regression as described in the previous chapter.

Estimation of fimbrial extension distances

Fimbria extensions were only calculated for the 'extra' data set as these videos contain reference beads. Immobilized reference beads are tracked using the conditions described in the previous chapter that were determined to be optimal for immobilized beads. Each video contains between 1-5 reference beads. The z-positions for these reference beads are averaged together and subtracted from the z-positions for the extension analysis only. Baseline drift was determined to be negligible for other bead characteristics examined, such as bead velocity.

The height of a bead before the initial application of force is determined from the average z-positions one second before the preload. The maximum extensions were estimated by averaging the largest two z-positions found within the first three seconds of force application and subtracting this average from the baseline. As the preload lasted only one second, the last two seconds were

at the lifetime force. For this extra data set, the lifetime force was always equal to or greater than the preload force. Only beads whose preload and lifetime force fell between 60 and 100 pN were kept for analysis.

Exponential Fits

Single exponential decay fit to lifetime data

A single exponential decay ($y = e^{(-k(f)t)}$) was fit the to the fraction of bonds remaining over time for each force bin using a maximum likelihood estimation. $k(f)$ was determined by dividing the total number of bonds detached in the collection period by the sum of the product of number of bonds that never detached and the total time of the collection period and the product of the total number of detached bonds and the average lifetime. The error was determined by dividing the value of $k(f)$ by the square root of the number of bonds that detached.

Double exponential decay fit to lifetime data

A double exponential decay ($y = ce^{(k(f)_{slow}t)} + (1-c)e^{(k(f)_{fast}t)}$) was fit to the 90% abbreviated survival curves using a least squares regression in Graph Pad Prism 9.0, where c is fraction of the fast state, and $k(f)_{fast}$ and $k(f)_{slow}$ are the force dependent rate constants for the fast and slow states. The value of c was initially fit independently to each force bin, then held constant for all force bins in a subsequent fit. Multiple initial guesses were tried for the fits and the values for both $k(f)$ remained constant for all force bins except for the lowest force bin.

Exponential fit to k(f) over force data

To estimate k^o and Δx for both the slow and fast an exponential curve, Bell's equation $y = k^o e^{(f \Delta x / k_B T)}$) was fit to the values of $k(f)_{slow}$ and $k(f)_{fast}$ over the average force of each bin using a least squares regression in Graph Pad Prism 9.0. The lowest force bin was excluded from this fit as the $k(f)$ values obtained are dependent on the initial guess and thus not trustworthy. A weighting scheme proportional to the inverse of the square of the value of $k(f)$ was used so the fit would not favor larger values of $k(f)$.

RESULTS

Measuring the lifetime of FimH

To measure the full lifetime of the high-affinity state of FimH, FimH-containing fimbria were immobilized on the floor of a magnetic tweezer chamber. Magnetic beads were functionalized with yeast mannan – a polysaccharide composed primarily of mannose, or bovine serum albumin (BSA) as a negative control. Using a bidirectional magnetic tweezer apparatus magnetic beads were brought to the chamber floor and allowed to interact with the surface for approximately two to three second. Afterward, an activating preload force was applied to the beads for one second to convert FimH into its high-affinity state. Beads that did not form a bond could be seen leaving the bottom surface of the chamber. BSA-coated beads adhered to the fimbria-coated surface in less than 1% of interactions (Figure 3.1A).

The preload forces applied ranged from 20-200 pN with the fraction of bonds surviving one second increasing with force, as expected given the FimH catch bond behavior (Figure 3.1A). Beads with a preload less than 60 pN were removed, because forces below this did not appear to be sufficient to activate the catch bond and we wanted to minimize the possibility of inactivated bonds. After the preload, the applied force was changed and held constant for the next 15 minutes. The time at which a bead detaches from the chamber floor is estimated by the frame in which a bead is at least 20 μm from the chamber floor or when the bead is clearly no longer on the chamber floor.

Beads are sorted into 20 pN bins and the bond lifetimes are reported as a survival plot (Figure 3.1B). As expected, the lifetimes of the bonds decrease as force increases. The catch bond behavior observed in the preload forces is no longer present, indicating the preload force successfully activated FimH into the high-affinity state.

We would expect the bond survival in each force bin would follow a single exponential decay that can be modeled by $B(t) = B(0) * e^{-k(f)t}$ [31] where *B(t)* is bonds left at time, *t* and *k(f)* is the unbinding rate at a given force. However, this model clearly does not fit the survival data well (Figure 3.1B). One reason for this poor fit could be multiple bonds interacting with each magnetic bead. This would cause the applied force to be distributed between the bonds, which would decrease the unbinding rate of the bond.

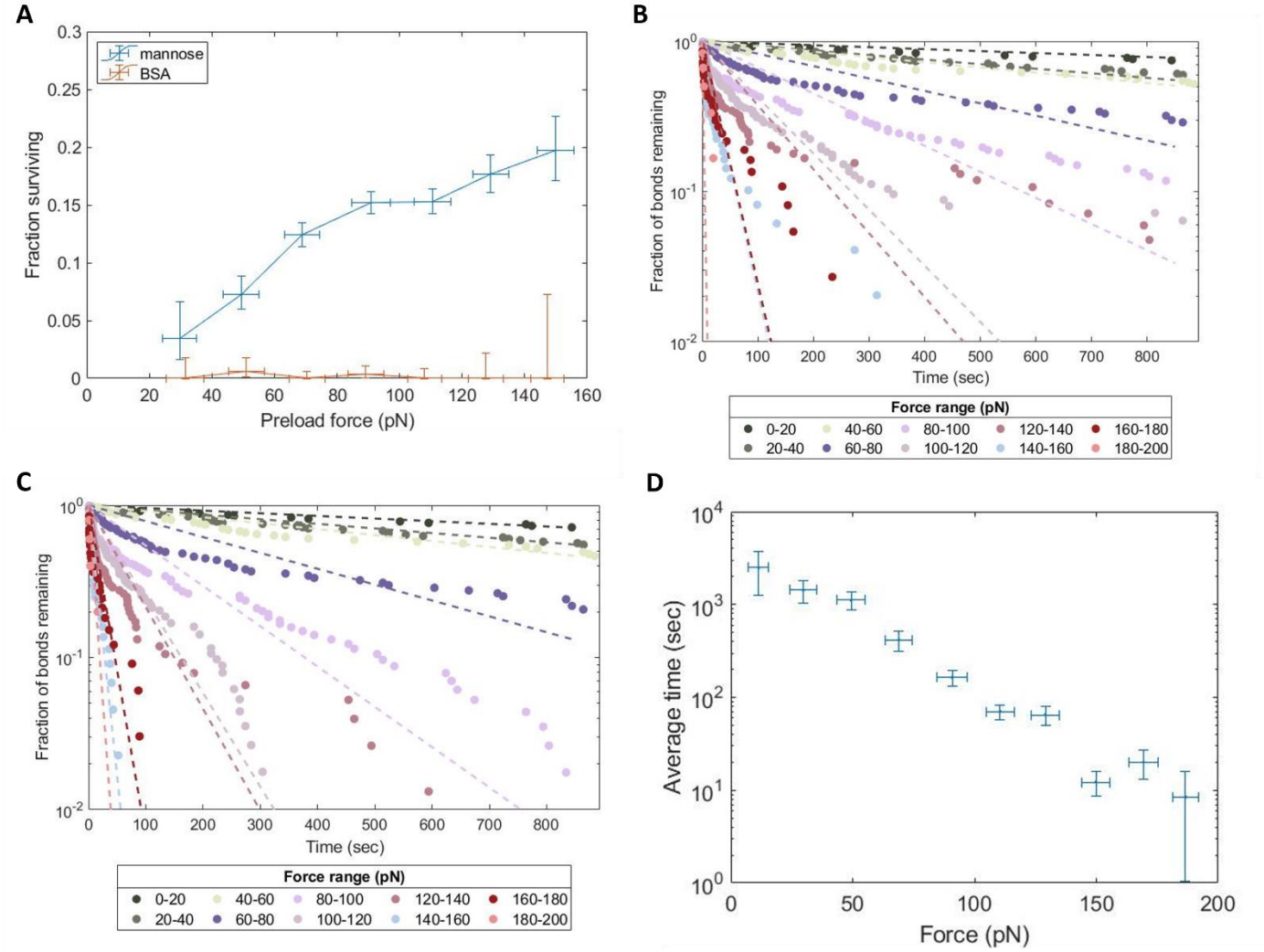

Figure 3.1. Lifetimes of the activated FimH mannose bond under force. (A) Fraction of mannose-coated and BSA-coated beads that were still adhered to the chamber floor after the preload force. Vertical error bars represent standard deviation assuming a binomial distribution. (B) Survival plot of FimH under different forces (points) fit with a single exponential decay model (dashed lines). (C) Lifetime data from A but with the 10% longest lived bonds removed (points). A single exponential decay was fit to this data set (dashed lines). (D) The average lifetime under force found by taking the inverse of the unbinding rates from D (*1/k(f)*). Vertical error bars represent 95% confidence interval. All horizontal error bars are the standard deviation of forces in the bin.

To ensure nearly all of the bonds formed in this assay were single molecule, the concentration of fimbria on the chamber surface was adjusted so that the approximately 20% of all beads that interacted with the surface adhered. We confirmed that on average, in our assay beads adhered with a fraction at or below 20% for all force bins in Figure 3.1A. Based on Poisson statistics at a 20% adhesion rate, approximately 10.8% of all attachments formed will form multiple bonds and at 15% this percent decreases to 8%[99]. Therefore, as the attachment rates of all

force bins are between 15 and 20%, only about 10% of all attachments should involve multiple bonds. To minimize the impact of these multiple bond interactions on the data, we removed the 10% longest lived bonds[101] and fit the exponential decay model to this abbreviated data set (Figure 3.1C).

The average lifetime (*1/k(f)*) for each force was determined based on the single-exponential decay fit (Figure 3.1D). At low force between 20-40 pN, the lifetime has a long-lived lifetime of 1400 seconds or over 20 minutes. However, given the poor fits of this model to the lifetime data in Figure 3.1C, these average lifetime estimations are likely not accurate.

Fimbrial extension analysis

In addition to using Poisson statistics, we sought an additional means to confirm whether our data contain multiple bonds per bead. FimH are located on the tip of fimbria, a filamentous organelle composed of a long coiled chain of proteins[35]. Uncoiled, fimbria have an average length of 1 μm and rarely are greater than 1.5 μm[35]. However, under forces greater than 60 pN, fimbria are capable of elongating up to 10 μm[35]. If a bead is attached to a single fimbria, the bead should appear to move a distance greater than 1 μm as the fimbria elongates under force. However, if a bead is attached to multiple bonds, the applied force would be distributed between all attachments and thus at least one, if not both fimbriae would be unable to uncoil and the bead would not move. It is important to note that since the fimbria are nonspecifically bound to the chamber floor, individual fimbria may be in an orientation in which they do not elongate a whole micrometer. Therefore, any beads that do not move at least one micrometer may still be single bonds. Nevertheless, we could still use the distance the fimbriae extend during the preload as a means to identify beads that must be attached to single bonds.

We could not accurately measure the preload extension distances in our initial lifetime data set, because the focus would drift, and we had no means to subtract the baseline. Therefore, we collected additional lifetime data, but used immobilized reference beads to measure the z-position of the baseline. We measured the distance the fimbria extended over three seconds. The data was filtered, keeping beads with both a preload and lifetime force between 60 pN and 110 pN. Under 60 pN of force, fimbriae uncoil at a rate of approximately 0.7 μm/sec and additional force increases the rate of uncoiling exponentially[35,67]. As 1 second may not be sufficient to see single fimbria

extend 1 μm, we also examined extensions two seconds into the lifetime measurement for a total of three seconds from the onset of force.

The extra lifetimes were divided into two force bins, 60-80 pN and 80-100 pN, to facilitate comparison to the initial data set. The new data is not statistically different from the lifetimes in Figure 3.1B for the corresponding bin as determined by a Log-rank test using GraphPad Prism 9.0 (Figure 3.2). With a 1 μm cutoff, the 60-80 pN force bin does not change noticeable. A larger extension cutoff though appears to make the survival plot take on a single exponential decay fit (Figure 3.2A). Removing all beads with an extension less than 1 μm for the 80-100 pN also appear to result in single exponential decay behavior (Figure 3.2B). For both force bins though, it is difficult to be sure if the reason for this apparent behavior is because mostly long-lived bonds were removed, or just because so many bonds in this data set failed to extend the total distance, regardless of their detachment time. It is possible that keeping only bonds that are certainly single result in a single exponential decay, but not enough data remains after the extension cutoff to be sure. We will need to collect additional data looking at extension distances to be more certain.

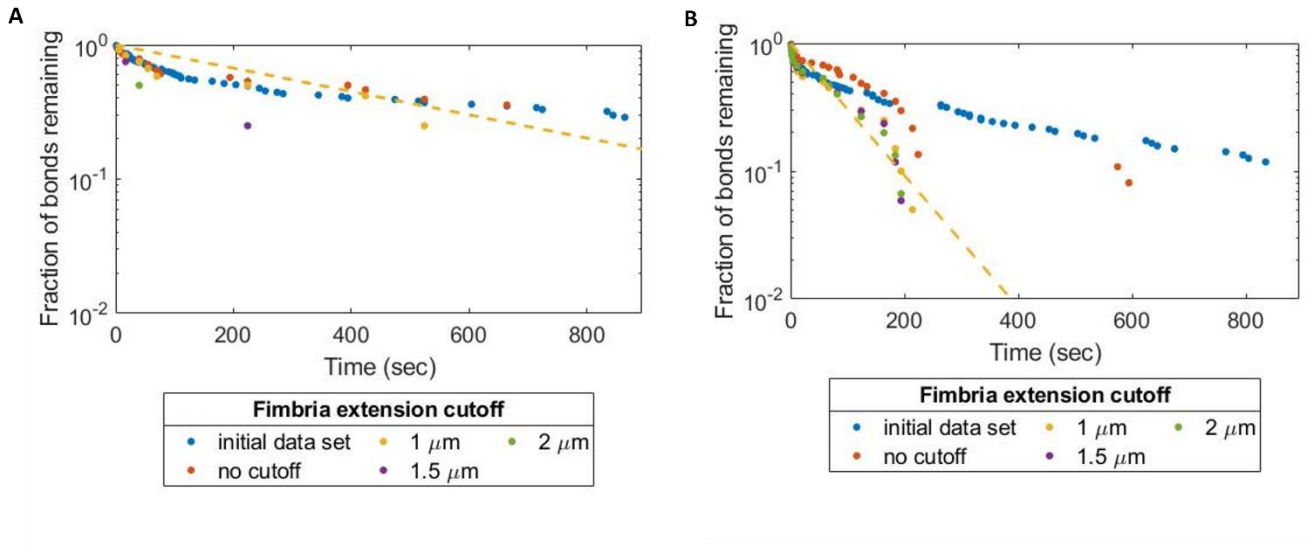

Figure 3.2. Survival plots of bonds filtered based on extension of fimbria for the (A) 60-80 pN bin and (B) 80-100 pN bin. Initial data set is the data of the corresponding bin Figure 3.1. Dotted lines are exponential decay fits of the 1 μm extension cutoff data set.

Double Exponential Decay Model

If the measured FimH lifetimes are mostly single molecule, this would suggest FimH is unbinding from two different states – on that unbinds faster, and one slower. Two explore this

possibility, we fit a double exponential decay model to the data, $B(t) = Ce^{-k_{fast}(f)\,t} + (1 - C)e^{-k_{slow}(f)t}$ where $k_{fast}(f)$ and $k_{slow}(f)$ are the unbinding constants of the two states under force and C is the proportion of the fast state in the population. This model is similar to the 2-state binding model proposed by Thomas et al to describe the FimH catch bond[7]. The model is fit to the data set from Figure 3.1C in which the 10% longest lived bonds have been removed and with different parameters for each force bin (Appendix Figure 1). The fit is greatly improved from the single exponential decay fit and appears to describe the data well.

Interestingly, the fraction of the fast state appears to increase with force from 0-60 pN, and above this force, the fraction is rather consistent (Appendix Figure 2). Given that less than 50% of the bonds break in the two lowest force bins, the estimated parameters for these bins are most likely to be erroneous. Therefore, we assumed the fraction of the fast state is the same for all force bins and fit the double exponential decay model with this assumption (Figure 3.3A). Nearly all bins were insensitive to the initial parameter guesses – only the 0-20 pN force bin changed with different initial guesses and thus the fit for this bin was deemed unreliable.

The resulting $k(f)$ values are shown in Figure 3.3B and increase exponentially with force. This relation can be modeled with Bell's equation[2,3], $k(f) = k^0 * e^{\frac{f\Delta x}{k_B T}}$ where $k(f)$ is the force dependent unbinding constant, k^o is the unbinding constant without force, Δx is the distance to the transition state and correlates with force sensitivity, and k_BT is the product of Boltzmann's constant and temperature, which equals 4.1 pN/nm at room temperature. The best fit parameters for the two equations are k^0_{fast} = 8.02E-4 sec^{-1}, Δx_{fast} = 0.197 nm, k^0_{slow} = 3.868E-5 sec^{-1}, Δx_{fast} = 0.189 nm. The values of $k(f)$ for the smallest force bin were excluded from this fit, as they are unreliable. The optimal percent of the fast state was 42%. The average lifetime under each force is estimated by $\frac{C}{k_{fast}} + \frac{1-C}{k_{slow}}$ (Figure 3.3C). These lifetimes are slightly higher than the ones predicted by the single exponential decay fit in Figure 3.1D with the 20-40 pN bin having an average time of 6500 seconds or 108 minutes.

To evaluate the quality of our fit we fit the double exponential decay model to the additional data set of lifetimes collected originally to analyze the extension distance of the fimbria. We removed the 10% longest lived bonds, as was done to the initial data set. We then determined the best fit $k(f)$ values for each force bin with C held constant at 0.42 and plotted this along with the fit found for the corresponding data set (Figure 3.3D). The parameters from the initial data set fit

the additional data set extremely well in the 60-80 pN bin range and the 95% confidence intervals (CI) of the new estimated parameters overlapped the 95% CI of the original data set's parameters (Appendix Table 1).

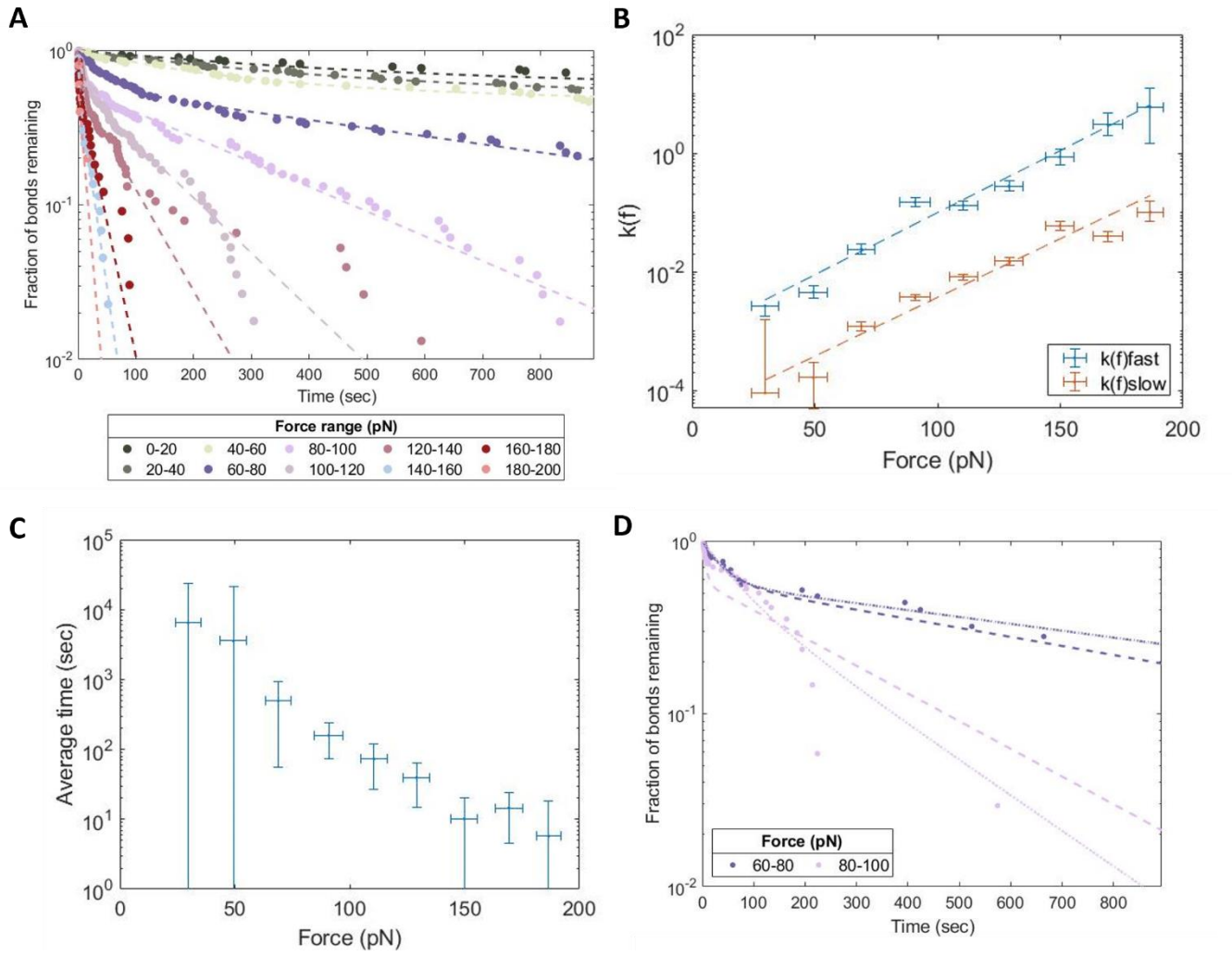

Figure 3.3. Double exponential decay fit (A) Double exponential decay fit (dotted lines) to survival data from Figure 1C. (B) *K(f)* values and (C) average lifetime from the fit. (D) Double exponential decay fit to the extra data set collected for figure 2 fit with the parameters found in part A (dashed lines) and the best fit parameters for this data set (dotted lines). Vertical error bars in B and C represent 95% confidence intervals. Some confidence interval bounds for the 20-40 pN bin could not be calculated. Horizontal error bars are the standard deviation of forces in the bin.

The parameters of the original data set for the 80-100 pN bin does not fit the new data as well as the other bin. However ,the estimated best *k(f)* values for this data set have overlapping (or

nearly overlapping) 95% CI with the *k(f)* of the original data set. Therefore, we have reasonably high confidence in the parameters of our double exponential decay fits.

DISCUSSION

Possible explanations for the double exponential decay unbinding behavior

Here we measure the unusually long lifetime of the FimH high-affinity state under force and find that the unbinding rates in our assay cannot be modeled by a single exponential decay function. Multiple fimbrial attachments to each bead could explain the complex unbinding kinetics measured[102]. This would cause the force felt on each fimbria to be less than expected, resulting in a slower unbinding rate. Our attempt to isolate single fimbria using extension distances is inconclusive about whether our data is caused by multiple bonds.

If the double-exponential unbinding rates are due to multiple bonds, then the slower-unbinding state of the fit could represent the fraction of multiple bonds and the faster-unbinding state is single bonds. Based on the resulting parameters from the double exponential decay fit, approximately 57% of detachment events would be due to multiple bonds. Based on our adhesion rate of 20% (Figure 3.1A), only about 10% of attachments should have formed multiple bonds. Since the longest lived 10% of bonds were removed from the data, we would expect the fraction of our data that is the result of multiple fimbria attachments to be negligible. For the data to be composed of over 50% of multiple bonds at an adhesion rate of 20%, the beads must not follow a Poisson distribution. For this to be possible, fimbria must not be binding independently in our assay.

However, it is highly unlikely that the presence of a FimH molecule influences the binding of other FimH. Only one FimH is known to be expressed on each fimbria[45] and isolated fimbria do not cluster[103]. Also, we do not suspect additional attachments are forming after the preload. During lifetime measurements additional attachments are unlikely to occur as force would cause the fimbria to lift off the surface, making the magnetic bead inaccessible to other fimbriae. While the ligand used, mannan contains chains of mannose, FimH only binds the terminal mannose of a chain and would not be able to reattach to another mannose subunit on the bead before force pulls the bead away.

The estimated fit parameters of the two states also do not make sense in the context of multiple bonds. The parameter describing the transition state of unbinding, Δx, for both the slow

and fast rates are nearly identical. This is not likely to be observed if multiple bonds are arranged in a parallel formation in which the force is distributed between all bonds and each bond breaks independently. The value of Δx of bound ruptures in this formation would be equal to the number of bonds divided by the Δx of a single bond[4]. Furthermore, if the fast state is caused by single fimbria attachments and the slow state by two fimbria attaching per bead, the ratio of $k°$ of the slow state to $k°$ of the fast state should be 3/2. However, the ratio of k° of the two states obtained from our fit is 20 Figure 3.4.

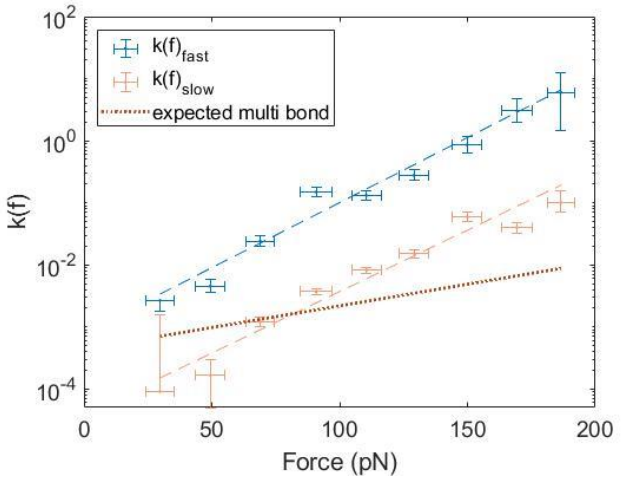

Figure 3.4. Estimated unbinding rates under force of multiple fimbria attached to a single bead. Assuming the fast state represents single fimbria attachments and the slow bond represents two fimbria attachments per bead, the *k(f)* of two fimbria is predicted using the $k°$ and Δx from the fast state and compared to the obtained *k(f)* for the slow state.

If our lifetime data is composed of single bonds, the multi-exponential decay behavior suggests there are at least two states of the force-activated FimH-mannose bond. A single state with two unbinding pathways would result in single exponential decay behavior of lifetimes over force with a rate from the combination of the unbinding rates of each pathway[7]. The similar values of Δx of the two states suggests that the energy barrier to unbinding may be similar and thus the mechanism of unbinding may be the same.

One explanation involves a mixed population of partially activated FimH. The FimH variant used, KB91,is characterized by a lower mannose affinity compared to other FimH variants[55]. Even when activated by discouraging association of the pilin and lectin domains via mutations, this variant is not fully activated into the high-affinity state, as detected by an antibody that recognizes this state (data not shown). Removal of the pilin domain and elongation of the lectin domain under force may not be sufficient to completely activate this variant either. Rather, the unbinding kinetics may represent a mixed population of partially and fully activated FimH.

Another cause for multi-state binding could involve the additional contacts FimH forms with residues outside of the mannose binding pocket. Hydrophobic and aromatic residues near the

binding pocket, including the tyrosine gate composed of Tyr48, Tyr137, are known to interact with moieties attached to a terminal mannose[50,53,104]. The ligand attached to the magnetic beads, mannan, is a polysaccharide composed of chains of mannan[105], and thus it can presumed that FimH is interacting with additional mannose residues beyond the terminal mannose. It is possible these additional contacts may be heterogeneous. The crystal structure of FimH bound to butyl mannoside showed one of the tyrosines of the tyrosine gate takes on at least two different orientations when bound to the ligand[50]. It is possible that additional mannose residues contact the tyrosine gate in different orientations, resulting in the observed multi-state behavior.

FimH has an unusually long lifetime under force

FimH has an extremely long-lived lifetime compared to other slip bonds and catch bonds. The lifetimes of many slip bonds reported in the literature are on the order 1 to 10 seconds at forces above 40 pN (Figure 3.5A). However, the high-affinity state of FimH has an average lifetime of 3500 seconds or almost one hour at 50 pN. The biotin-streptavidin bond is the only receptor-ligand interaction we know of that has measured lifetimes longer than FimH under moderate forces. Gruber et al. measured lifetimes of biotin bound to each of the four streptavidin subunits, while anchoring one subunit to the surface. The relation of the bonding subunit to the anchored subunit greatly affected the lifetimes, resulting in three distinct lifetime trends for the four subunits. Two of these trends demonstrate longer lifetimes under force than FimH while the third – which is attributed to two different subunits – is shorter-lived[106]. The lifetime of biotin and streptavidin under force depends on the geometry of the tether and the applied force[106,107] and so a large range of lifetimes have been reported in the literature. The biotin/streptavidin lifetimes in Figure 3.5A are the longest we found in the literature, but there have been many measurements reported that estimate the lifetime under force to be much shorter compared to the FimH/mannose lifetimes[30,108,109]. Even if the longest-lived lifetimes of FimH are due to multiple bonds and only the faster state represents single bonds, the lifetime is unusually long. $1/k(f)_{fast}$ is over 200 seconds at 50 pN, which is still faster than the lifetimes measured for most slip bonds (Figure 3.5A).

Catch bond lifetimes are often analyzed by measuring the lifetime under various forces without an activating preload. Since we only measured the lifetimes of FimH in the high-affinity state, we cannot directly compare these lifetimes to the maximum lifetimes of catch bonds in the literature, as our assay does not consider the effect of the low-affinity state on the average lifetime.

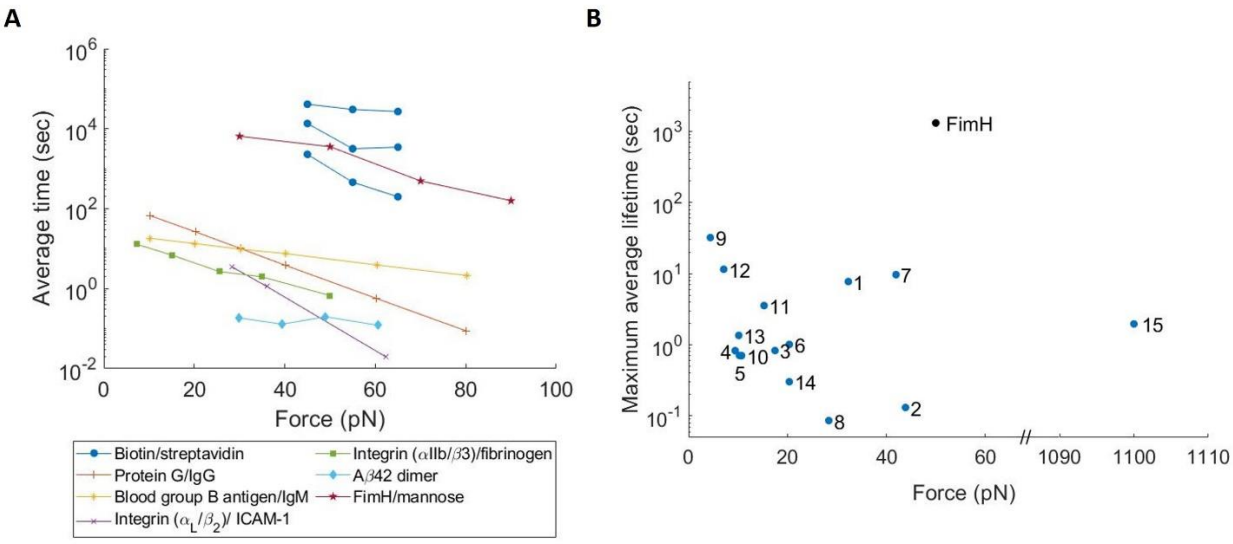

Figure 3.5. Comparison of the influence of force on the lifetime of other non-covalent bonds to FimH. (A) Average slips bond lifetimes under force. Three different lifetimes were measured for biotin/streptavidin due to the different subunits of streptavidin. Only the lifetime of the high-affinity state of FimH is considered. Sources: Biotin/streptavidin[106], Protein G/IgG[110], Blood group B antigen/IgM[110], Integrin αL/β2/ ICAM-1[101], Integrin αII/β3/ fibrinogen[111], Aβ42 dimer[112]. (B) The average lifetimes of FimH are estimated by multiplying the normalized bead adhesion rate at each force by the average lifetime and the maximum is shown in black. 1. Integrin (α5β1)/fibronectin[113]* 2. L-selectin/PSGL-1[34] 3. Self1/sulfate[114] 4. T-cell receptor/MHC[115] 5.G-actin/G-actin[116] 6. G-actin/F-actin[116] 7. Fibrin/fibrinogen[111] 8. E-cadherin/E-cadherin[22] 9. Actin/myosin[13117] 10. P-selectin/PSGL-1[118] 11. Integrin(αLβ2)/ICAM-1[119] 12. Vinculin/actin[120] 13. Cadherin-catenin/actin[121] 14. GP1bα/VWF[122] 15. SpsD/fibrinogen[123]
*lifetime may not have been fully measured.

The total lifetime is equal to the sum of the average lifetime for the low-affinity and high-affinity states multiplied by the respective proportion of each state[7]. We can approximate the fraction of FimH activated in the high-affinity state at each force by dividing the fraction of bonds in Figure 3.1A by the bin with the highest fraction (0.198). We then multiplied these fractions by the lifetimes in Figure 3.3C to approximate the average lifetime of the FimH catch bond under force. We are assuming every force bin had the same bond adhesion rate, all FimH bonds were in the high-affinity state at the force bin with the highest adhesion, and that a negligible number of high-affinity bonds unbound during the 1 second preload. Since the low-affinity state is known to last less than one second, the contribution this state would have to the overall lifetimes would be negligible. The adjusted average lifetimes peak at a force between 40 and 60 pN, which is comparable to what has been seen in previous lifetime experiments[45]. This maximum lifetime

though, is over 1,000 seconds which is over an order of magnitude larger than the maximum lifetimes of most other catch bonds reported in the literature (Figure 3.5B).

The kinetochore microtubule complex, which possesses a catch bond-like property, reaches a maximum lifetime of about 3,000 seconds[94], which does exceed our estimated maximum lifetime of FimH. However, this maximum lifetime is achieved at a force between 3-5 pN [94] – an order of magnitude less than the force required to activate the FimH catch bond. Furthermore this complex involves more interactions than a receptor ligand bond[124]. FimH possesses a remarkably long lifetime for a receptor-ligand interaction under large forces.

The extremely long lifetimes of FimH may be necessary to mediate E. coli's adhesion to host epithelial cells. Initial attachment of fimbria to a mannosylated surface appears to occur via a single fimbria and additional fimbriae do not attach for at least several seconds, if not longer[7]. The long lifetimes of activated FimH, may provide a means that ensures bacteria can remain attached to the surface long enough before entering the host cell or forming biofilms. Knowing the full lifetime of FimH of under force can help elucidate the mechanism of bacterial attachment and infection in fluid environments.

APPENDIX

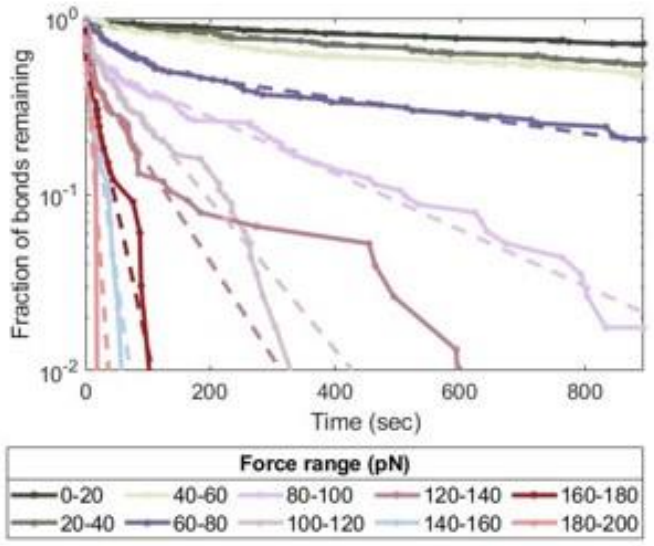

Appendix Figure 1. Double exponential decay fit to survival plot without removing the longest lived 10%

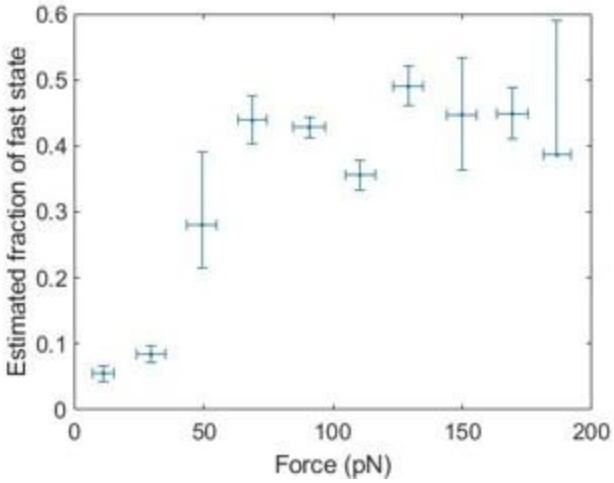

Appendix Figure 2. Fraction of fast state estimated from the double exponential fit, with this parameter was fit independently for each bin. Vertical error bars represent 95% confidence interval. Horizontal error bars are standard deviation of forces in the force bin.

Appendix Table 1. Comparison of confidence intervals of estimated values of $k(f)_{fast}$ and $k(f)_{slow}$ using the initial data set and additional data set

	60 - 80 pN				80 -100 pN			
	Initial data set		Additional data set		Initial data set		Additional data set	
	value	95% CI	value	95% CI	value	95% CI	value	95% CI
$k(f)_{fast}$	2.40E-02	2.0E-02 to 2.9E-02	2.70E-02	2.2E-02 to 3.3E-2	1.50E-01	1.2E-01 to 1.6E-01	1.53E-02	2.3E-3 to 1.0E-01
$k(f)_{slow}$	1.20E-03	1.0E-03 to 1.4E-03	9.20E-04	7.4E-04 to 1.1E-3	3.70E-03	3.3E-03 to 4.1E-03	4.72E-03	2.8E-03 to 1.9E-02

Chapter 4. CONCLUSION

In this work we proposed and implemented a solution to improve tracking of mobile magnetic spheres that was later applied to measuring the lifetime of FimH in a magnetic tweezer assay. In contrast to other evaluation techniques which measure the precision of tracking on an immobilized bead, we measured the error in position measurements of a moving bead. We found that tracking a mobile bead resulted in much larger error than tracking a static bead, demonstrating that conventional means of evaluation of a particle tracking technique are insufficient for estimating the error associated with a moving bead. We were able to significantly reduce the error by excluding the center-most region of the bead from analysis, although we were still unable to reduce the total error to just that of an immobilized bead. Measurement of velocity of a mobile bead is commonly used to estimate the force applied to a magnetic bead in a magnetic tweezer assay. Our improvements to LUT tracking reduced the error of velocity measurements by over 30%.

We then applied this improved tracking methodology to a magnetic tweezer assay which, for the first time, measured the lifetime of the high-affinity state of FimH under force and demonstrated that the lifetime of this catch bond far outlasts the lifetimes of other catch bonds in the literature. In our assay these lifetimes do not fit the expected single-exponential behavior that is characteristic of single-state unbinding kinetics. As our results could not be described by the predicted behavior of multiple fimbria attachments, we strongly believe we measured single molecule unbinding kinetics of mannose from FimH in the high-affinity state. Therefore, my data showed for the first time, heterogeneity in the FimH-mannose bond after activation of force.

In addition to the work presented in these chapters, I also contributed to various collaborators' projects. In one instance I developed the assay protocol used to measure real-time binding kinetics[125]. For another work I collected and analyzed the binding kinetics of FimH adhesion to antibodies[126]. Finally, I also measured and compared the average rupture strength of wild-type and mutants of FimH to evaluate how the mutations influenced the maximum binding strength of FimH. In conclusion the work performed in my dissertation has contributed to magnetic tweezer usage and improved our understanding of a model catch bond's kinetics.

BIBLIOGRAPHY

1. Sokurenko E V., Vogel V, Thomas WE. Catch bond mechanism of force-enhanced adhesion: counter-intuitive, eluside but...widespread? *Cell Host Microbe*. 2008;4(4):314-323. doi:10.1016/j.chom.2008.09.005.
2. Bell GI. Models for the specific adhesion of cells to cells. *Science (80-)*. 1978. doi:10.1126/science.347575
3. Evans E. Probing the relation between force - Lifetime - And chemistry in single molecular bonds. *Annu Rev Biophys Biomol Struct*. 2001;30:105-128. doi:10.1146/annurev.biophys.30.1.105
4. Isabey D, Féréol S, Caluch A, Fodil R, Louis B, Pelle G. Force distribution on multiple bonds controls the kinetics of adhesion in stretched cells. *J Biomech*. 2013;46(2):307-313. doi:10.1016/j.jbiomech.2012.10.039
5. Pereverzev Y V., Prezhdo O V., Forero M, Sokurenko E V., Thomas WE. The two-pathway model for the catch-slip transition in biological adhesion. *Biophys J*. 2005. doi:10.1529/biophysj.105.062158
6. Dembo M, Torney DC, Saxman K, Hammer D. *The Reaction-Limited Kinetics of Membrane-to-Surface Adhesion and Detachment*. Vol 234.; 1988. https://www.jstor.org/stable/36290. Accessed March 19, 2019.
7. Thomas WE, Forero M, Yakovenko O, et al. Catch-bond model derived from allostery explains force-activated bacterial adhesion. *Biophys J*. 2006;90(3):753-764. doi:10.1529/biophysj.105.066548
8. Pereverzev Y V., Prezhdo O V., Forero M, Sokurenko E V., Thomas WE. The two-pathway model for the catch-slip transition in biological adhesion. *Biophys J*. 2005;89(3):1446-1454. doi:10.1529/biophysj.105.062158
9. Rakshit S, Zhang Y, Manibog K, Shafraz O, Sivasankar S. Ideal, catch, and slip bonds in cadherin adhesion. *Proc Natl Acad Sci*. 2012;109(46):18815-18820. doi:10.1073/pnas.1208349109
10. Kong F, García AJ, Mould AP, Humphries MJ, Zhu C. Demonstration of catch bonds between an integrin and its ligand. *J Cell Biol*. 2009;185(7):1275-1284. doi:10.1083/jcb.200810002
11. Marshall BT, Long M, Piper JW, Yago T, McEver RP, Zhu C. Direct observation of catch bonds involving cell-adhesion molecules. *Nature*. 2003;423(6936):190-193. doi:10.1038/nature01605
12. Yago T, Wu J, Wey CD, Klopocki AG, Zhu C, Mcever RP. Catch bonds govern adhesion through L-selectin at threshold shear. *J Cell Biol*. 2004;166(6):913-923. doi:10.1083/jcb.200403144
13. Guo B, Guilford WH. Mechanics of actomyosin bonds in different nucleotide states are tuned to muscle contraction. *Proc Natl Acad Sci*. 2006;103(26):9844-9849. doi:10.1073/pnas.0601255103
14. Yakovenko O, Nunez J, Bensing B, et al. Serine-Rich Repeat Adhesins Mediate Shear-Enhanced Streptococcal Binding to Platelets. *Infect Immun*. 2018;86(6). doi:10.1128/iai.00160-18
15. Thomas WE, Trintchina E, Forero M, Vogel V, Sokurenko E V. *Bacterial Adhesion to Target Cells Enhanced by Shear Force*. Vol 109.; 2002. https://ac.els-cdn.com/S0092867402007961/1-s2.0-S0092867402007961-main.pdf?_tid=25713add-

30d8-498a-bab7-50b611e588d&acdnat=1533922478_4783f3e53edc639224d8c8ef79c9947d.
16. Yakovenko O, Tchesnokova V, Sokurenko E V., Thomas WE. Inactive conformation enhances binding function in physiological conditions. *Proc Natl Acad Sci*. 2015;112(32):9884-9889. doi:10.1073/pnas.1503160112
17. Sokurenko E V., Chesnokova V, Dykhuizen DE, et al. Pathogenic adaptation of Escherichia coli by natural variation of the FimH adhesin. *Proc Natl Acad Sci U S A*. 1998;95(15):8922-8926. doi:10.1073/pnas.95.15.8922
18. Nilsson LM, Thomas WE, Sokurenko E V, Vogel V. Elevated Shear Stress Protects Escherichia coli Cells Adhering to Surfaces via Catch Bonds from Detachment by Soluble Inhibitors †. *Appl Environ Microbiol*. 2006;72(4):3005-3010. doi:10.1128/AEM.72.4.3005-3010.2006
19. Anderson BN, Ding AM, Nilsson LM, et al. Weak Rolling Adhesion Enhances Bacterial Surface Colonization. *J Bacteriol*. 2007;189(5):1794-1802. doi:10.1128/JB.00899-06
20. Wang J huai. T cell receptors, mechanosensors, catch bonds and immunotherapy. *Prog Biophys Mol Biol*. 2020;153:23-27. doi:10.1016/j.pbiomolbio.2020.01.001
21. Lou J, Zhu C. A structure-based sliding-rebinding mechanism for catch bonds. *Biophys J*. 2007;92(5):1471-1485. doi:10.1529/biophysj.106.097048
22. Rakshit S, Zhang Y, Manibog K, Shafraz O, Sivasankar S. Ideal, catch, and slip bonds in cadherin adhesion. *Proc Natl Acad Sci*. 2012;109(46):18815-18820. doi:10.1073/pnas.1208349109
23. Rakshit S, Sivasankar S. Biomechanics of cell adhesion: how force regulates the lifetime of adhesive bonds at the single molecule level. *Phys Chem Chem Phys*. 2014;16(6):2211. doi:10.1039/c3cp53963f
24. Liu Z, Liu H, Vera AM, Bernardi RC, Tinnefeld P, Nash MA. High force catch bond mechanism of bacterial adhesion in the human gut. *Nat Commun*. 2020;11(1):1-12. doi:10.1038/s41467-020-18063-x
25. Sauer MM, Jakob RP, Eras J, et al. Catch-bond mechanism of the bacterial adhesin FimH. *Nat Commun*. 2016;7:10738. doi:10.1038/ncomms10738
26. Yakovenko O, Sharma S, Forero M, et al. FimH forms catch bonds that are enhanced by mechanical force due to allosteric regulation. *J Biol Chem*. 2008;283(17):11596-11605. doi:10.1074/jbc.M707815200
27. Manibog K, Sankar K, Kim S-A, Zhang Y, Jernigan RL, Sivasankar S. Molecular determinants of cadherin ideal bond formation: Conformation-dependent unbinding on a multidimensional landscape. *Proc Natl Acad Sci*. 2016;113(39):E5711-E5720. doi:10.1073/pnas.1604012113
28. Merkel R, Nassoy P, Leung A, Ritchie K, Evans E. Energy landscapes of receptor-ligand bonds explored with dynamic force spectroscopy. *Nature*. 1999;397(6714):50-53. doi:10.1038/16219
29. Sarangapani KK, Qian J, Chen W, et al. Regulation of catch bonds by rate of force application. *J Biol Chem*. 2011;286(37):32749-32761. doi:10.1074/jbc.M111.240044
30. Rico F, Chu C, Moy VT. Force-Clamp Measurements of Receptor–Ligand Interactions. *Methods Mol Biol*. 2011;736:331-353. doi:10.1007/978-1-61779-105-5_20
31. Thomas W. Catch Bonds in Adhesion. *Annu Rev Biomed Eng*. 2008;10(1):39-57. doi:10.1146/annurev.bioeng.10.061807.160427
32. Evans E, Leung A, Heinrich V, Zhu C. Mechanical switching and coupling between two

dissociation pathways in a P-selectin adhesion bond. *Proc Natl Acad Sci U S A*. 2004;101(31):11281-11286. doi:10.1073/pnas.0401870101

33. Thomas WE, Vogel V, Sokurenko E. Biophysics of catch bonds. *Annu Rev Biophys*. 2008;37(1):399-416. doi:10.1146/annurev.biophys.37.032807.125804
34. Sarangapani KK, Yago T, Klopocki AG, et al. Low Force Decelerates L-selectin Dissociation from P-selectin Glycoprotein Ligand-1 and Endoglycan. *J Biol Chem*. 2004;279(3):2291-2298. doi:10.1074/jbc.M310396200
35. Forero M, Yakovenko O, Sokurenko E V, Thomas WE, Vogel V. Uncoiling mechanics of Escherichia coli type I fimbriae are optimized for catch bonds. *PLoS Biol*. 2006;4(9):1509-1516. doi:10.1371/journal.pbio.0040298
36. Schembri MA, Kjaergaard K, Sokurenko E V., Klemm P. Molecular characterization of the Escherichia coli FimH adhesin. *J Infect Dis*. 2001;183(Supplement 1):S28-31. doi:10.1086/318847
37. Choudhury D, Thompson A, Stojanoff V, et al. X-ray structure of the FimC-FimH chaperone-adhesin complex from uropathogenic escherichia coli. *Science (80-)*. 1999;285:1061-1066.
38. Aprikian P, Interlandi G, Kidd BA, et al. The bacterial fimbrial tip acts as a mechanical force sensor. *PLoS Biol*. 2011;9(5). doi:10.1371/journal.pbio.1000617
39. Whitfield M, Thomas WE. A nanoadhesive composed of receptor-ligand bonds. *J Adhes*. 2011;87(5):427-446. doi:10.1080/00218464.2011.575311
40. Sokurenko E V., Chesnokova V, Doyle RJ, Hasty DL. Diversity of the Escherichia coli Type 1 Fimbrial Lectin. *J Biol Chem*. 1997;272(28):17880-17886.
41. Anderson GG, Dodson KW, Hooton TM, Hultgren SJ. Intracellular bacterial communities of uropathogenic Escherichia coli in urinary tract pathogenesis. *Trends Microbiol*. 2004;12(9):424-430. doi:10.1016/j.tim.2004.07.005
42. Zhou G, Mo W, Sebbel P, Min G, Neubert TA, Glockshuber R. Uroplakin Ia is the urothelial receptor for uropathogenic Escherichia coli : evidence from in vitro FimH binding. 2001.
43. Aprikian P, Tchesnokova V, Kidd B, et al. Interdomain interaction in the FimH adhesin of Escherichia coli regulates the affinity to mannose. *J Biol Chem*. 2007;282(32):23437-23446. doi:10.1074/jbc.M702037200
44. Interlandi G, Thomas WE. Mechanism of allosteric propagation across a β-sheet structure investigated by molecular dynamics simulations. *Proteins Struct Funct Bioinforma*. 2016;84(7):990-1008. doi:10.1002/prot.25050
45. Le Trong I, Aprikian P, Kidd BA, et al. Structural Basis for Mechanical Force Regulation of the Adhesin FimH via Finger Trap-like b Sheet Twisting. *Cell*. 2010;141(4):645-655. doi:10.1016/j.cell.2010.03.038
46. Rodriguez VB, Kidd BA, Interlandi G, Tchesnokova V, Sokurenko E V., Thomas WE. Allosteric coupling in the bacterial adhesive protein FimH. *J Biol Chem*. 2013;288(33):24128-24139. doi:10.1074/jbc.M113.461376
47. Nilsson LM, Thomas WE, Sokurenko E V., Vogel V. Beyond Induced-Fit Receptor-Ligand Interactions : Structural Changes that Can Significantly Extend Bond Lifetimes. *Cell*. 2008;16:1047-1058. doi:10.1016/j.str.2008.03.012
48. Nilsson LM, Thomas WE, Sokurenko E V., Vogel V. Beyond Induced-Fit Receptor-Ligand Interactions: Structural Changes that Can Significantly Extend Bond Lifetimes. *Cell*. 2008;16(7):1047-1058. doi:10.1016/j.str.2008.03.012

49. Rabbani S, Krammer EM, Roos G, et al. Mutation of Tyr137 of the universal Escherichia coli fimbrial adhesin FimH relaxes the tyrosine gate prior to mannose binding. *IUCrJ*. 2017;4:7-23. doi:10.1107/S2052252516016675
50. Bouckaert J, Berglund J, Schembri M, et al. Receptor binding studies disclose a novel class of high-affinity inhibitors of the Escherichia coli FimH adhesin. *Mol Microbiol*. 2005;55(2):441-455. doi:10.1111/j.1365-2958.2004.04415.x
51. Bouckaert J, Mackenzie J, De Paz JL, et al. The affinity of the FimH fimbrial adhesin is receptor-driven and quasi-independent of Escherichia coli pathotypes. *Mol Microbiol*. 2006;61(6):1556-1568. doi:10.1111/j.1365-2958.2006.05352.x
52. Wellens A, Garofalo C, Nguyen H, et al. Intervening with urinary tract infectious using anti-adhesives based on the crystal structure of the FimH-oligomannose-3 complex. *PLoS One*. 2008;3(4). doi:10.1371/journal.pone.0002040
53. Wellens A, Lahmann M, Touaibia M, et al. The tyrosine gate as a potential entropic lever in the receptor-binding site of the bacterial adhesin FimH. *Biochemistry*. 2012;51(24):4790-4799. doi:10.1021/bi300251r
54. Sokurenko E V., Schembri MA, Trintchina E, Kjærgaard K, Hasty DL, Klemm P. Valency conversion in the type 1 fimbrial adhesin of Escherichia coli. *Mol Microbiol*. 2001;41(3):675-686. doi:10.1046/j.1365-2958.2001.02545.x
55. Sokurenko E V., Courtney HS, Maslow J, Siitonen A, Hasty DL. Quantitative differences in adhesiveness of type 1 fimbriated Escherichia coli due to structural differences in fimH genes. *J Bacteriol*. 1995;177(13):3680-3686. doi:10.1128/jb.177.13.3680-3686.1995
56. Thomas WE, Nilsson LM, Forero M, Sokurenko E V., Vogel V. Shear-dependent "stick-and-roll" adhesion of type 1 fimbriated Escherichia coli. *Mol Microbiol*. 2004;53(5):1545-1557. doi:10.1111/j.1365-2958.2004.04226.x
57. Whitfield M, Ghose T, Thomas WE. Shear-stabilized rolling behavior of E. coli examined with simulations. *Biophys J*. 2010;99(8):2470-2478. doi:10.1016/j.bpj.2010.08.045
58. Wu M, Roberts JW, Kim S, Koch DL, Delisa MP. Collective Bacterial Dynamics Revealed Using a Three-Dimensional Population-Scale Defocused Particle Tracking Technique. *Appl Environ Microbiol*. 2006;72(7):4987-4994. doi:10.1128/AEM.00158-06
59. Dulin D, Cui TJ, Cnossen J, Docter MW, Lipfert J, Dekker NH. High Spatiotemporal-Resolution Magnetic Tweezers: Calibration and Applications for DNA Dynamics. *Biophys J*. 2015;109(10):2113-2125. doi:10.1016/j.bpj.2015.10.018
60. Löf A, Walker PU, Sedlak SM, et al. Multiplexed protein force spectroscopy reveals equilibrium protein folding dynamics and the low-force response of von Willebrand factor. *Proc Natl Acad Sci*. 2019;116(38):201901794. doi:10.1073/pnas.1901794116
61. Bornfleth H, Edelmann P, Zink D, Cremer T, Cremer C. Quantitative motion analysis of subchromosomal foci in living cells using four-dimensional microscopy. *Biophys J*. 1999;77(5):2871-2886. doi:10.1016/S0006-3495(99)77119-5
62. Heinrich V, Wong WP, Halvorsen K, Evans E. Imaging biomolecular interactions by fast three-dimensional tracking of laser-confined carrier particles. *Langmuir*. 2008;24(4):1194-1203. doi:10.1021/la7027059
63. Kou L, Jin L, Lei H, et al. Real-time parallel 3D multiple particle tracking with single molecule centrifugal force microscopy. *J Microsc*. 2019;273(3):178-188. doi:10.1111/jmi.12773
64. Makarchuk S, Beyer N, Gaiddon C, Grange W, Hébraud P. Holographic Traction Force Microscopy. *Sci Rep*. 2018;8(1):1-11. doi:10.1038/s41598-018-21206-2

65. Zhao X, Zeng X, Lu C, Yan J. Studying the mechanical responses of proteins using magnetic tweezers. *Nanotechnology*. 2017;28(41):414002. doi:10.1088/1361-6528/aa837e
66. Ribeck N, Saleh OA. Multiplexed single-molecule measurements with magnetic tweezers. *Rev Sci Instrum*. 2008;79:94301. doi:10.1063/1.2981687
67. Johnson KC, Clemmens E, Mahmoud H, Kirkpatrick R, Vizcarra JC, Thomas WE. A multiplexed magnetic tweezer with precision particle tracking and bi-directional force control. *J Biol Eng*. 2017;11(1). doi:10.1186/s13036-017-0091-2
68. Kollmannsberger P, Fabry B. High-force magnetic tweezers with force feedback for biological applications. *Rev Sci Instrum*. 2007;78(11):4561. doi:10.1063/1.2804771
69. Carter BC, Shubeita GT, Gross SP. Tracking single particles: A user-friendly quantitative evaluation. *Phys Biol*. 2005;2:60-72. doi:10.1088/1478-3967/2/1/008
70. Cheezum MK, Walker WF, Guilford WH. Quantitative comparison of algorithms for tracking single fluorescent particles. *Biophys J*. 2001;81(4):2378-2388. doi:10.1016/S0006-3495(01)75884-5
71. Zhang Z, Menq C-H. Three-dimensional particle tracking with subnanometer resolution using off-focus images. *Appl Opt*. 2008;47(13):2361-2370. doi:10.1364/AO.47.002361
72. Lee S-H, Roichman Y, Yi G-R, et al. Characterizing and tracking single colloidal particles with video holographic microscopy. *Opt Express*. 2007;15(26):18275. doi:10.1364/oe.15.018275
73. Van Loenhout MTJ, Kerssemakers JWJ, De Vlaminck I, Dekker C. Non-bias-limited tracking of spherical particles, enabling nanometer resolution at low magnification. *Biophys J*. 2012;102(10):2362-2371. doi:10.1016/j.bpj.2012.03.073
74. Brouwer TB, Hermans N, van Noort, J1. Brouwer, T.B., N. Hermans and J van N 2020. MN 3D T of MU an F-PABJ 118:2245–2257. oh. Multiplexed Nanometric 3D Tracking of Microbeads Using an FFT-Phasor Algorithm. *Biophys J*. 2020;118(9):2245-2257. doi:10.1016/j.bpj.2020.01.015
75. Cnossen JP, Dulin D, Dekker NH. An optimized software framework for real-time, high-throughput tracking of spherical beads. *Rev Sci Instrum*. 2014;85(10):0-10. doi:10.1063/1.4898178
76. Del Rio A, Perez-Jimenez R, Liu R, Roca-Cusachs P, Fernandez JM, Sheetz MP. Stretching single talin rod molecules activates vinculin binding. *Science (80-)*. 2009;323(5914):638-641. doi:10.1126/science.1162912
77. Rief M, Gautel M, Oesterhelt F, Fernandez JM, Gaub HE. Reversible unfolding of individual titin immunoglobulin domains by AFM. *Science (80-)*. 1997;276(5315):1109-1112. doi:10.1126/science.276.5315.1109
78. Haber C, Wirtz D. Magnetic tweezers for DNA micromanipulation. *Rev Sci Instrum*. 2000;71(12):4561-4570. doi:10.1063/1.1326056
79. Kovari DT, Dunlap D, Weeks ER, Finzi L. Model-free 3D localization with precision estimates for brightfield-imaged particles. *Opt Express*. 2019;27(21):29875-29895. doi:10.1364/oe.27.029875
80. Parthasarathy R. Rapid, accurate particle tracking by calculation of radial symmetry centers. *Nat Methods*. 2012;9(7):724-726. doi:10.1038/nmeth.2071
81. Abraham A V, Ram S, Chao J, Ward ES, Ober RJ. Quantitative study of single molecule location estimation techniques. *Opt Express*. 2009;17(26):23352-23373. http://www4.utsouthwestern.edu/wardlab/EstimationTool. Accessed November 18, 2020.
82. Lansdorp BM, Tabrizi SJ, Dittmore A, Saleh OA. A high-speed magnetic tweezer beyond

10,000 frames per second. *Rev Sci Instrum*. 2013;84(4):0-5. doi:10.1063/1.4802678
83. Ghosh RN, Webb WW. Automated detection and tracking of individual and clustered cell surface low density lipoprotein receptor molecules. *Biophys J*. 1994;66(5):1301-1318. doi:10.1016/S0006-3495(94)80939-7
84. Carlucci L, Johnson KC, Thomas WE. Three dimensional bead tracking. 2021. doi:10.5281/zenodo.4724130
85. Cheng P, Jhiang SM, Menq CH. Real-time visual sensing system achieving high-speed 3D particle tracking with nanometer resolution. *Appl Opt*. 2013;52(31):7530-7539. doi:10.1364/AO.52.007530
86. Yago K. THE MECHANICAL AND COLLOIDAL PROPERTIES OF AMOEBA PROTOPLASM A N D THEIR RELATIONS TO THE MECHANISM OF AMOEBOID MOVEMENT. *Comp Biochem Physiol*. 1961;3:77-91.
87. Maude AD. End effects in a falling-sphere viscometer. *Br J Appl Phys*. 1961;12:293-295. https://iopscience.iop.org/article/10.1088/0508-3443/12/6/306/pdf. Accessed August 29, 2019.
88. Chio CC, Tse Y-LS. Hindered Diffusion near Fluid−Solid Interfaces: Comparison of Molecular Dynamics to Continuum Hydrodynamics. 2020. doi:10.1021/acs.langmuir.0c01228
89. Goldman AJ, Cox RG, Brenner H. Slow viscous motion of a sphere parallel to a plane wall-Motion through a quiescent fluid. *Chem Eng Sci*. 1967;22(4):653-660. doi:10.1016/0009-2509(67)80048-4
90. Bausch AR, Möller W, Sackmann E. Measurement of local viscoelasticity and forces in living cells by magnetic tweezers. *Biophys J*. 1999;76(1 I):573-579. doi:10.1016/S0006-3495(99)77225-5
91. Wang X, Luo M, Wu H, et al. A Three-Dimensional Magnetic Tweezer System of Intraembryonic Navigation and Measurement. *IEEE Trans Robot*. 2018;34(1):240-247.
92. Wang X, Ho C, Tsatskis Y, et al. Intracellular manipulation and measurement with multipole magnetic tweezers. *Sci Robot*. 2019;4. doi:10.1126/scirobotics.aav6180
93. Tchesnokova V, Aprikian P, Yakovenko O, et al. Integrin-like allosteric properties of the catch bond-forming FimH adhesin of Escherichia coli. *J Biol Chem*. 2008;283(12):7823-7833. doi:10.1074/jbc.M707804200
94. Akiyoshi B, Sarangapani KK, Powers AF, et al. Tension directly stabilizes reconstituted kinetochore-microtubule attachments. *Nature*. 2010;468(7323):576-579. doi:10.1038/nature09594
95. Chen W, Evans E, McEver RP, Zhu C. Monitoring receptor-ligand interactions between surfaces by thermal fluctuations. *Biophys J*. 2008;94(2):694-701. doi:10.1529/biophysj.107.117895
96. Popa I, Kosuri P, Alegre-Cebollada J, Garcia-Manyes S, Fernandez JM. Force dependency of biochemical reactions measured by single-molecule force-clamp spectroscopy. *Nat Protoc*. 2013;8(7):1261-1276. doi:10.1038/nprot.2013.056
97. Tanase M, Biais N, Sheetz M. Magnetic Tweezers in Cell Biology. *Methods Cell Biol*. 2007;83:473-493. doi:10.1016/S0091-679X(07)83020-2
98. Snook JH, Guilford WH. A high-throughput technique reveals the load-and site density-dependent kinetics of e-selectin. *Cell Mol Bioeng*. 2012;5(4):493-503. doi:10.1007/s12195-012-0247-6
99. Johnson KC, Thomas WE. How Do We Know when Single-Molecule Force Spectroscopy

Really Tests Single Bonds? *Biophys J*. 2018;114(9):2032-2039. doi:10.1016/j.bpj.2018.04.002
100. Gosse C, Croquette V. Magnetic tweezers: Micromanipulation and force measurement at the molecular level. *Biophys J*. 2002;82(6):3314-3329. doi:10.1016/S0006-3495(02)75672-5
101. Evans E, Kinoshita K, Simon S, Leung A. Long-lived, high-strength states of ICAM-1 bonds to β2integrin, I: Lifetimes of bonds to recombinant αLβ2under force. *Biophys J*. 2010;98(8):1458-1466. doi:10.1016/j.bpj.2009.09.067
102. Zhu C, Long M, Chesla SE, Bongrand P. Measuring receptor/ligand interaction at the single-bond level: Experimental and interpretative issues. *Ann Biomed Eng*. 2002;30(3):305-314. doi:10.1114/1.1467923
103. Hahn E, Wild P, Hermanns U, et al. Exploring the 3D molecular architecture of Escherichia coli type 1 pili. *J Mol Biol*. 2002;323(5):845-857. doi:10.1016/S0022-2836(02)01005-7
104. Bouckaert J, Mackenzie J, De Paz JL, et al. The affinity of the FimH fimbrial adhesin is receptor-driven and quasi-independent of Escherichia coli pathotypes. *Mol Microbiol*. 2006;61(6):1556-1568. doi:10.1111/j.1365-2958.2006.05352.x
105. Jones GH, Ballou CE. Studies on the Structure of Yeast Mannan. *J Biol Chem*. 1969;244(4):1043-1051. doi:10.1021/ja01191a021
106. Gruber S, Löf A, Sedlak SM, Benoit M, Gaub HE, Lipfert J. Designed anchoring geometries determine lifetimes of biotin-streptavidin bonds under constant load and enable ultra-stable coupling. *Nanoscale*. 2020;12(41):21131-21137. doi:10.1039/d0nr03665j
107. Sedlak SM, Schendel LC, Gaub HE, Bernardi RC. Streptavidin/biotin: Tethering geometry defines unbinding mechanics. *Sci Adv*. 2020;6(13). doi:10.1126/sciadv.aay5999
108. Jeney S, Mor F, Koszali R, Forró L, Moy VT. Monitoring ligand–receptor interactions by photonic force microscopy. *Nanotechnology*. 2010;21(25):255102. doi:10.1088/0957-4484/21/25/255102
109. Litvinov RI, Weisel JW. Shear strengthens fibrin: the knob-hole interactions display "catch-slip" kinetics. *J Thromb Haemost*. 2014;4(1):139-148. doi:10.1038/nmeth.2839.A
110. Kwong D, Tees DFJ, Goldsmith HL. Kinetics and Locus of Failure of Receptor-Ligand-Mediated Adhesion Between Latex Spheres. II. Protein-Protein Bond. *Biophys J*. 1996;71:1115-1122. doi:10.1016/S0006-3495(96)79313-X
111. Litvinov RI, Barsegov V, Schissler AJ, et al. Dissociation of bimolecular αIIbβ3-fibrinogen complex under a constant tensile force. *Biophys J*. 2011;100(1):165-173. doi:10.1016/j.bpj.2010.11.019
112. Maity S, Lyubchenko YL. Force clamp approach for characterization of nano-assembly in amyloid beta 42 dimer. *Nanoscale*. 2019;11(25):12259-12265. doi:10.1039/c9nr01670h
113. Kong F, Mould AP, Humphries MJ, Zhu C. Demonstration of catch bonds between an integrin and its ligand. *J Cell Biol*. 2009;185(7):1275-1284. doi:10.1083/jcb.200810002
114. Harder A, Möller AK, Milz F, et al. Catch bond interaction between cell-surface sulfatase sulf1 and glycosaminoglycans. *Biophys J*. 2015;108(7):1709-1717. doi:10.1016/j.bpj.2015.02.028
115. Liu B, Chen W, Evavold BD, Zhu C. Accumulation of dynamic catch bonds between TCR and agonist peptide-MHC triggers T cell signaling. *Cell*. 2014;157(2):357-368. doi:10.1016/j.cell.2014.02.053

116. Lee CY, Lou J, Wen KK, et al. Actin depolymerization under force is governed by lysine 113:glutamic acid 195-mediated catch-slip bonds. *Proc Natl Acad Sci U S A*. 2013;110(13):5022-5027. doi:10.1073/pnas.1218407110
117. Guo B, Guilford WH. Mechanics of actomyosin bonds in different nucleotide states are tuned to muscle contraction. *Proc Natl Acad Sci U S A*. 2006;103(26):9844-9849. doi:10.1073/pnas.0601255103
118. Marshall BT, Long M, Piper JW, Yago T, McEver RP, Zhu C. Direct observation of catch bonds involving cell-adhesion molecules. *Nature*. 2003;423(6936):190-193. doi:10.1038/nature01605
119. Chen W, Lou J, Evans E, Zhu C. Observing force-regulated conformational changes and ligand dissociation from a single integrin on cells. *J Cell Biol*. 2012;199(3):497-512. doi:10.1083/jcb.201201091
120. Huang D, Bax N, Buckley C, Weis W, Dunn A. Vinculin forms a Catch Bond with F-Actin that Depends on Actin Filament Orientation. *Science (80-)*. 2017;357:703-706. doi:10.1016/j.bpj.2016.11.1453
121. Buckley CD, Tan J, Anderson KL, et al. The minimal cadherin-catenin complex binds to actin filaments under force. *Science (80-)*. 2014;346(6209):600-609. doi:10.1126/science.1254211
122. Yago T, Lou J, Wu T, et al. Platelet glycoprotein Ibα forms catch bonds with human WT vWF but not with type 2B von Willebrand disease vWF. *J Clin Invest*. 2008;118(9):3195-3207. doi:10.1172/JCI35754
123. Mathelié-Guinlet M, Viela F, Pietrocola G, Speziale P, Alsteens D, Dufrêne YF. Force-clamp spectroscopy identifies a catch bond mechanism in a Gram-positive pathogen. *Nat Commun*. 2020;11:5431. doi:10.1038/s41467-020-19216-8
124. Asbury CL, Tien JF, Davis TN. Kinetochores' gripping feat: Conformational wave or biased diffusion? *Trends Cell Biol*. 2011;21(1):38-46. doi:10.1016/j.tcb.2010.09.003
125. Ludwig SG, Kiyohara CL, Carlucci LA, Kisiela D, Sokurenko E V, Thomas WE. FimH as a scaffold for regulated molecular recognition. *J Biol Eng*. 2021;15(1). doi:10.1186/s13036-020-00253-2
126. Kisiela DI, Magala P, Interlandi G, et al. Toggle switch residues control allosteric transitions in bacterial adhesins by participating in a concerted repacking of the protein core. *PLoS Pathog*. 2021;17(4). doi:10.1371/journal.ppat.1009440

VITA

Laura Ann Carlucci

Education

University of Washington, Seattle, Wa **Sept 2021**
Ph.D., Bioengineering

University of Massachusetts, Amherst, Ma **May 2016**
B.S., Biochemistry and Molecular Biology
Summa Cum Laude, Phi Beta Kappa

Research Experience

Graduate Research Assistant, *University of Washington, Seattle, WA* **2017- Present**
Advisor: Dr. Wendy Thomas

Undergraduate Research Assistant, *University of Massachusetts, Amherst, MA* **2012-2016**
Advisor: Dr. Tobias Baskin

Undergraduate Summer Intern, *Ames National Laboratory, Ames, IA* **Summer 2015**
Advisor: Dr. Young-Jin Lee

Undergraduate Summer Intern, *Rutgers University, New Brunswick, NJ* **Summer 2014**
Advisor: Dr. Donald Winkelmann

Grants and Fellowships

Molecular Biophysics Training Grant **2017**
University of Washington Hurd Fellowship **2016**
University of Massachusetts Commonwealth Honors College Research Grant **2015**
University of Massachusetts Junior Fellow **2015**

Publications

Carlucci L.A. and Thomas W.E. Modification to axial tracking of mobile magnetic microspheres. Manuscript submitted for publication.

Kisiela, D.I., Magala, P., Interlandi, G., **Carlucci, L.A.,** Ramos, A., Tchesnokova, V., Basanta, B., Yarov-Yarovoy, V., Avagyan, H., Hovhannisyan, A., Thomas, W.E., Stenkamp, R.E., Klevit, R.E., Sokurenko, E.V. Toggle switch residues control allosteric transitions in bacterial adhesins by participating in a concerted repacking of the protein core. *PLOS Pathogens*. 17, 4. 2021.

Gupta Ludwig, S., Kiyohara, C.L., **Carlucci, L.A.,** Kisiela, D., Sokurenko, E.V., Thomas,W.E.. FimH as a Scaffold for Regulated Molecular Recognition. *Journal of Biological Engineering* 15, 2. 2021.

Dueñas M.E., **Carlucci L.,** Lee Y.J. Matrix Recrystallization for MALDI-MS Imaging of Maize Lipids at High-Spatial Resolution. *Journal of the American Society for Mass Spectrometry*. 27(9):1575-1578. 2016.

Talks and Poster Presentations

Carlucci, L. and Thomas, W. Influence of Force on the FimH Catch Bond.
Platform presented at Biophysical Society 65th Annual Meeting; 2021 February 28; Virtual.

Carlucci, L. and Thomas, W. Mechanical Strength of Catch Bond Forming FimH and Mannose.
Platform presented at Biophysical Society 63rd Annual Meeting; 2019 March 4; Baltimore, MD.

Carlucci, L. and Thomas, W. Influence of Force on the *E. coli* Adhesin, FimH.
Poster presented at Cell Bio Virtual 2020; 2020 December 15; Virtual.

Carlucci, L. and Thomas, W. Influence of Mechanical Force on the Lifetime of Activated FimH-Mannose Bond.

Poster presented at: 33rd Annual Protein Society Symposium; 2019 July 1; Seattle, Wa, UW Bioengineering 2019 Annual Retreat; 2019 September 19; Seattle, Wa (2nd place), 2019 Seattle Cell Science Symposium; 2019 December 13 and Biophysical Society 64th Annual Meeting; 2020 March 19; San Diego, CA.

Carlucci, L. and Baskin, T. I. Localization of Pectin and Hemicellulose in Plant Cell Walls Using Immunogold Labeling With Scanning Electron Microscopy.

Poster presented at: 22nd Massachusetts Statewide Undergraduate Research Conference; 2016 April 22; Amherst, Ma and Life Science Symposium; 2016 April 27; Amherst, Ma

Teaching Experience

Teaching Assistant, University of Washington **Spring 2020, 2021**

Computational Bioengineering

Graduate mentor **2018- 2019**

Mentored undergraduates on laboratory practices and critical thinking

Teaching Assistant, University of Washington **Fall 2017**

Biochemistry

Campus and Community Involvement

Authored white paper for Washington State Legislature **2020**

Collaborated with Washington Academy of Sciences on a white paper about human gene editing

Admissions committee member **2020**

Volunteer tutor **2019**

Tutored middle school children at the local Somali community center

Leadership experience

Chemical Hygiene Officer, *University of Washington, Seattle Washington* **2020 - Present**

Prepared lab space for annual inspection and manage lab safety trainings of lab members

Fencing Coach, *Salle Auriol Seattle Fencing Club, Seattle Washington* **2018-2019**

Taught a class of approximately 10 students introductory fencing